Journal of Cleaner Production 351 (2022) 131470

Contents lists available at ScienceDirect

Journal of Cleaner Production

journal homepage: www.elsevier.com/locate/jclepro

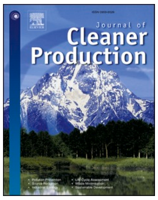

Numerical analysis of feedforward concepts for advanced control of organic Rankine cycle systems on heavy-duty vehicles

Roberto Pili [a,*], Christoph Wieland [b,c], Hartmut Spliethoff [b,d], Fredrik Haglind [a]

[a] Department of Mechanical Engineering, Technical University of Denmark, Nils Koppels Allé, Building 403, 2800, Kongens Lyngby, Denmark
[b] Technical University of Munich, Chair of Energy Systems, Boltzmannstr. 15, 85748, Garching bei München, Germany
[c] Technical University of Munich, Munich School of Engineering, Lichtenbergstr. 4a, 85748, Garching bei München, Germany
[d] Bavarian Center for Applied Energy Research, Walther-Meißner-Straße 6, 85748, Garching bei München, Germany

ARTICLE INFO

Handling Editor: Panos Seferlis

Keywords:
Organic Rankine cycle
Heavy-duty vehicle
Advanced control
Feedforward

ABSTRACT

Organic Rankine cycle systems are the most promising technology to recover the waste heat from heavy-duty vehicles in an efficient and economical way, thus increasing their energy efficiency and reducing their environmental impact. A major challenge for an efficient and profitable integration of the organic Rankine cycle unit is presented by the highly transient nature of the waste heat during a driving cycle. In order to cope with the rapid fluctuations of the waste heat and to ensure safe operation, advanced control techniques have gained particular attention in the last decade. This paper presents novel high-order advanced feedforward control concepts for organic Rankine cycle units that improve the performance of classical proportional integral controllers. The proposed approach enables the use of high-order nonlinear models for feedforward control of organic Rankine cycle systems, therefore allowing for more accurate estimation of the desired control action. As a reference, a proportional integral controller with feedforward is presented, acting on the pump mass flow rate to control the degree of superheating at the turbine inlet, which is a key variable to ensure high power output and safe operation of the organic Rankine cycle system. Static, linear and nonlinear dynamic inversed-model feedforward controllers were integrated with a classical proportional integral controller and numerically evaluated under a realistic waste heat profile of a heavy-duty truck. The results suggest that the static and the linear feedforward concepts do not offer any advantages compared with the classical proportional integral controller, because they result in a higher absolute mean square tracking error and a higher cumulative controller effort. Instead, the high-order nonlinear dynamic inversed-model feedforward controller introduced in this work offers important advantages compared with the classical proportional integral controller by reducing the absolute root mean square tracking error from 10.8 K to 2.2 K without excessively increasing the controller cumulative effort (limited to 1.9%/s). On the contrary, the classical proportional integral controller could optimize only one of the objectives at the expenses of the other. The proposed control approach significantly improves the operation of the organic Rankine cycle unit, limiting the fluctuations of the degree of superheating and keeping this quantity within ±7 K of the desired set point. Thus, the novel feedforward concept will be highly beneficial in integrating classical proportional integral control of organic Rankine cycle units that involve highly transient heat sources.

1. Introduction

Heavy-duty vehicles contribute to more than one-quarter of the CO_2-emissions from road transport, and approximately 5% of the total greenhouse gas emissions in the European Union (European Environmental Ag, 2018). In order to reduce the environmental impact of heavy-duty vehicles, the European Council developed a regulation that entered into force on 14 August 2019 and obliges truck manufacturers to cut the average CO_2-emissions by 15% from 2025 onwards and by 30% from 2030 onwards compared to 2019 and 2020, respectively (Regulation () 2019/, 2019). A significant reduction of the CO_2-emissions from trucks can be achieved by increasing the energy efficiency of the diesel internal combustion engines used as the powertrain for the trucks (Carstensen et al., 2019; Delgado and Lutsey, 2014). In fact, more than 50% of the input fuel energy is released unused to the atmosphere in the form of waste heat. The available waste heat is found in the exhaust gas

---

* Corresponding author.
E-mail address: robpi@mek.dtu.dk (R. Pili).

https://doi.org/10.1016/j.jclepro.2022.131470
Received 11 November 2021; Received in revised form 27 February 2022; Accepted 19 March 2022

at medium temperature (200–600 °C), while the remaining part is transferred to the environment through the engine coolant loop (<100 °C) and the charge air cooler (<200 °C) (Lion et al., 2017; Amicabile et al., 2015; Dolz et al., 2012; Teng et al., 2007).

The organic Rankine cycle (ORC) technology constitutes an appropriate solution to recover the waste heat and convert it into mechanical or electrical power in an efficient way (Macchi and Astolfi, 2017; Sprouse and Depcik, 2013; Quoilin et al., 2013). These systems are similar to classical steam Rankine cycle units, but use an organic working fluid with higher molecular weight and lower boiling point than water, thus achieving a better efficiency at low and medium temperatures of the waste heat (Teng et al., 2007). They are also beneficial for small-scale applications (from a few kW_e to 10 MW_e) with respect to steam Rankine cycles, especially in regard to the design of the expander, which can reach a high efficiency with a limited number of expansion stages (Macchi and Astolfi, 2017). Moreover, ORC units show a better part-load performance (de la Fuente and Greig, 2015; Andreasen et al., 2017), which is of crucial importance to maximize the net power output of the waste heat recovery unit, given the fact that the waste heat conditions fluctuate over a broad range during the driving cycle (Lion et al., 2017). The fluctuations are highly transient, posing significant challenges to the dynamics and control of the ORC system (Seitz et al., 2016). In fact, alongside the maximization of the net power output, several constraints need to be guaranteed during the ORC operation (Tona and Peralez, 2015; Hernandez et al., 2014; Rathod et al., 2019; Koppauer et al., 2018): i) the temperature of the working fluid has to be kept below its thermal degradation limit; ii) the pressure has to be kept below its maximum allowed by the mechanical components; iii) the pump has to be operated avoiding cavitation and within its operational limits; and iv) in the case of the turbo-expander, a positive degree of superheating at turbine inlet has to be ensured to avoid erosion of the blades and poor expander isentropic efficiency.

The complexity of simultaneously satisfying the aforementioned constraints and the objective of maximizing the net power output have motivated researchers to investigate several control ideas, both numerically and experimentally. An extensive review of the main challenges and control concepts developed for the ORC technology is presented in Ref. (Imran et al., 2020). Proportional-integral-derivative (PID) controllers are the most common type of controllers used in industry, thanks to their simplicity and robustness (Corriou, 2004). Although some control strategies with PID have been proposed (Quoilin et al., 2011; Marchionni et al., 2018; Pili et al., 2019a; Xu et al., 2020a), it has been highlighted that large deviations from the desired degree of superheating can occur when the ORC is subjected to the rapid waste heat fluctuations of truck engines (Imran and Haglind, 2019; Feru et al., 2014). In the attempt of improving the control performance, several authors have studied advanced control concepts, like linear quadratic regulators (LQR), non-Gaussian control (NGC) and model predictive control (MPC).

A LQR has the advantage of using a simple, fast algorithm, and is able to handle multivariable systems with very limited computational effort (Luong and Tsao, 2014a; Zhang et al., 2012a). As a drawback, the algorithm is based on model linearization and does not consider the nonlinear couplings among the degree of superheating, the evaporation pressure and other relevant quantities typical of ORC units. In addition, a proper choice of tuning parameters in the design of LQR controllers is required to ensure stable and high-performing operation, which implies a time-consuming tuning procedure. Examples of LQR control for waste heat recovery ORC systems can be found in Refs (Luong and Tsao, 2014a). and (Zhang et al., 2012a).

NGC aims to minimize the entropy function and the mean value of the squared tracking error, by assuming a non-Gaussian disturbance (Zhang et al., 2012b). As a drawback, the NGC solution is based on a time-consuming, multi-objective optimization that needs to be solved in real-time (Zhang et al., 2016a, 2018). Furthermore, this option has only been tested in a very limited operational range and requires a more general assessment based on realistic heat source conditions.

MPC techniques have recently been gaining more attention (Hernandez et al., 2014, 2015, 2016; Koppauer et al., 2018; Feru et al., 2014; Luong and Tsao, 2014a; Grelet et al., 2015a; Zhang et al., 2016b). MPC is also based on linearization as LQR but it uses a receding horizon approach to define its control action. In other words, it does not optimize the control action for an infinite operational time window, but only for a limited prediction horizon. At every time step, the optimization is repeated for the next prediction horizon. It is not clear what the best tuning parameters for the MPC are, although work is has been developed to provide general guidelines for MPC tuning (Pili et al., 2021). Overall, the MPC concepts proposed in literature could typically outperform classical PID controllers (and LQR in Ref (Luong and Tsao, 2014b).), but their performance has in almost all cases been evaluated based only on small step changes or far from realistic driving conditions (Tona and Peralez, 2015; Hernandez et al., 2014, 2015, 2016; Zhang et al., 2016b; Liu et al., 2017). Furthermore, it is unclear whether the gains achievable with the MPC solution justify its increased complexity and computational costs (Vaupel et al., 2021). By using a nonlinear model of the ORC system and avoiding the approximations resulting from linearization, the nonlinear MPC has the potential for better performance, but the real-time implementation of this technique over a realistic heat source profile raises concerns regarding the required computational effort (Koppauer et al., 2018; Feru et al., 2014; Liu et al., 2017; Petr et al., 2015; Wu et al., 2019).

In contrast to the mentioned advanced control solutions, the classical feedback/feedforward control scheme can offer important advantages compared with the LQR, NGC and MPC approaches:

- The feedback/feedforward controller does not require an online optimization. Instead, it is based on the inversion of an existing model. This considerably improves the feasibility for real-time control;
- Recent research reported that the advantages provided by nonlinear MPC with respect to a feedback/feedforward structure are below 2% in terms of average ORC net power output, raising concerns whether such small gains justify the increased complexity, implementation and computational costs of nonlinear MPC (Vaupel et al., 2021). Since nonlinear MPC is one of the most powerful control approaches available, lower or equivalent improvement margins should be expected for LQR, NGC and MPC;
- The extension from linear to nonlinear models with high accuracy does not imply considerable increase in computational effort, since no optimization has to be carried out like in NGC and MPC;
- The low-order nonlinear feedforward models in Refs (Peralez et al., 2013, 2017; Seitz et al., 2018). can be extended to high-order nonlinear models with simple modifications, as presented in this work. This allows for the usage of more accurate models than those in LQR and MPC, which are based on linearization, without considerably increasing the computation time as in NGC and nonlinear MPC;
- Uncertainties due to modeling, measurement errors or system aging can easily be compensated by the feedback part, whereas the feedforward contributes to most of the control action.

Although conceptually very simple, there is only a very limited number of studies on the application of feedforward control of ORC systems, and only seven of them deal with waste heat recovery from heavy-duty vehicles (Vaupel et al., 2021; Peralez et al., 2013, 2017; Padula et al., 2012; Usman et al., 2017; Xu et al., 2020b; Keller et al., 2020). A dynamic inversed-model feedforward was investigated in Refs (Peralez et al., 2013, 2017). to control the degree of superheating at the turbine inlet of an ORC unit using R245fa as the working fluid. The feedforward action was based on a third-order moving boundary (MB) model of the ORC evaporator, which was inverted. In this way, the mass flow rate of the pump could be determined from the given desired degree of superheating. The solution was tested experimentally on a realistic profile of the exhaust gases. The results indicated that the controller with feedforward could significantly improve the performance compared with the use of the PID controller only, with a maximum error in the degree of superheating of 1.9 K with respect to the set point. Similar numerical results were achieved in Ref. (Grelet et al., 2015b). Given the very promising results of the dynamic inversed-model feedforward, a similar concept was presented in Ref. (Seitz et al., 2018). The feedforward model was this time a fourth-order MB evaporator coupled with a volumetric expander. The results suggested much larger oscillations in the degree of superheating (- 15/+60 K from the set point) than those presented in Ref. (Peralez et al., 2017). Nonetheless, the option using a gain-scheduled LQR integrated to the feedforward could achieve at least 25% higher thermal-to-electric efficiency than the other investigated options, such as static feedforward or dynamic feedforward with PI feedback. Keller et al. (2020) compared a PID controller combined with static feedforward with a MPC concept. The authors found that large oscillations in the evaporator outlet temperature occurred with the feedback/feedforward concept, while the MPC could keep a mean absolute error to 4.5 K over a transient heat source profile. Vaupel et al. (2021) compared nonlinear MPC solutions with a conventional PI/feedforward control. The feedforward concept was based on a linear filter acting on an offline steady-state optimized estimation of the mass flow rate as a function of the mass flow rate and inlet temperature of the exhaust gas. Based on a highly transient waste heat profile, the nonlinear MPC solutions could reach 0.5% higher net power output than the conventional PI/feedforward concept. By assuming perfect prediction of the waste heat profile, an improvement of about 2% could be achieved. Given the low improvements of the nonlinear MPC concepts with respect to the PI/feedforward control, which would amount to an absolute increase in engine performance of 0.1%, the authors conclude that, even if the real-time capability of nonlinear MPC could be achieved onboard, it might not be worthwhile to invest in the high development costs compared to the PI-feedforward solution.

Given the positive results of dynamic inversed-model feedforward controllers (coupled with PID or LQR feedback control) that were reported in literature, this solution is a promising option to reject the fluctuations of the exhaust gases of truck internal combustion engines and keep the operation of the ORC unit close to the desired set point. However, the large deviations of the operation of the ORC unit from the desired set point found in Ref (Seitz et al., 2018). suggest that further research is required to improve the controller performance of nonlinear feedforward concepts, guaranteeing safe and efficient operation in real applications. Deviations of approximately 10 K were also found with the linear filtering concept in Ref. (Vaupel et al., 2021), and even larger deviations were reported by using the static feedforward concept in Ref. (Keller et al., 2020). High-order MB models of the evaporator are typically more accurate than the static feedforward model in Ref (Keller et al., 2020). and the low-order models used in Refs. (Vaupel et al., 2021; Peralez et al., 2013, 2017; Seitz et al., 2018), and these could be used to improve the performance of the feedforward controller in terms of tracking and disturbance rejection. However, the mathematical conditions necessary for the direct inversion of the higher-order MB models do not hold, because the high-order MB models are non-minimum phase (Peralez et al., 2012). Therefore, numerical approximations are required for this approach to be successful. The lack of methods that allow for satisfying the mathematical conditions required for developing nonlinear feedforward concepts based on high-order models has so far hindered the use of high-order models.

This paper presents novel advanced feedforward control concepts for ORC units recovering waste heat from the exhaust gas of a heavy-duty truck. The main contribution of the paper is the novel approach used to integrate dynamic nonlinear inversed-model feedforward to a classical PI control system, while considering high-order MB models together with innovative numerical approximations. In the analysis, we quantify the cumulative control effort that, although very important for the controller tuning, was typically neglected or not quantified in previous works in the field of control of ORC power systems. In particular, the new numerical approximations modify the mass accumulation term in the energy balance of the two-phase and vapor regions, thus allowing for more accurate feedforward action and effective control. The nonlinear inversed-model feedforward controller was integrated and compared with a classical PI feedback controller. Alternative feedforward concepts such as a static feedforward controller and a linear gain-scheduled feedforward controller were also compared. The ORC evaporator was approximated by a FV model of the ORC evaporator developed in Dymola (Systèmes, 2020) and imported in Simulink® (MathWorks®. Simulink® 201, 2019). The FV model was chosen as the reference test system, because it has proven to be more accurate than the MB model for the simulation of ORC evaporators (Wei et al., 2008). The feedforward control concepts were also developed in the Simulink® environment, but they were based on a MB model of the ORC evaporator, given its lower complexity and computational load. As a reference, a single-input-single-output PI controller with feedforward is presented, acting on the pump mass flow rate to control the degree of superheating at the turbine inlet, which is a key variable for the safe operation of the ORC system. For the analyzed control concepts, we present the trade-off between the minimization of the deviations from the desired set point and the cumulative controller effort. The performance of the controllers was evaluated by considering exhaust gas measurements provided by a truck manufacturer of a heavy-duty truck operating on a 45-min trip. At last, it is important to highlight that the control concepts presented in the paper can also be applied to other fields, including ORC plants that supply both heat and electric power (Pili et al., 2020a), heat pumps (Meesenburg et al., 2020), and thermal systems in general, which are subject to large variations of the heat source, heat sink or electro-mechanical load.

The paper is divided into five sections. The design of the ORC system under study is presented in section 2; the dynamic modeling of the ORC system is described in section 3, while the controller development is presented in section 4; the results are presented in section 5, followed by an outline of the conclusions in section 6.

2. Design of the organic Rankine cycle system

This section describes the design of the ORC system considered in this work, together with the waste heat profile of the engine of the heavy-duty vehicle.

2.1. Plant layout

The case study considered in this work consists of a simple ORC power system recovering waste heat from the exhaust tailpipe of a heavy-duty truck. The plant layout is depicted in Fig. 1. The exhaust gas reaches the ORC after the post-treatment system (selective catalytic reactor) at point 1g, where harmful components and particles are removed. By transferring heat to the ORC unit, the gas is cooled down to point 2g, and it is then released to the environment through the tailpipe. A three-way valve is included to bypass the heat exchanger/evaporator (EVA), if needed to avoid overloading of the ORC unit. A simple ORC unit is shown on the right-hand side of Fig. 1. A simple configuration without a recuperator is chosen to guarantee the compactness and simplicity that are required to install the ORC onboard the truck cabin. The working fluid is forwarded by a pump (P) from the liquid state 0 to the evaporator (EVA) inlet at state 1, where the working fluid is preheated, vaporized and superheated up to state 2. The superheated vapor enters the turbine (T), where the thermo-mechanical conversion occurs. The working fluid exits the turbine at state 3, where it is condensed in the condenser (CO) to saturated liquid at state 0, thus closing the thermodynamic cycle.

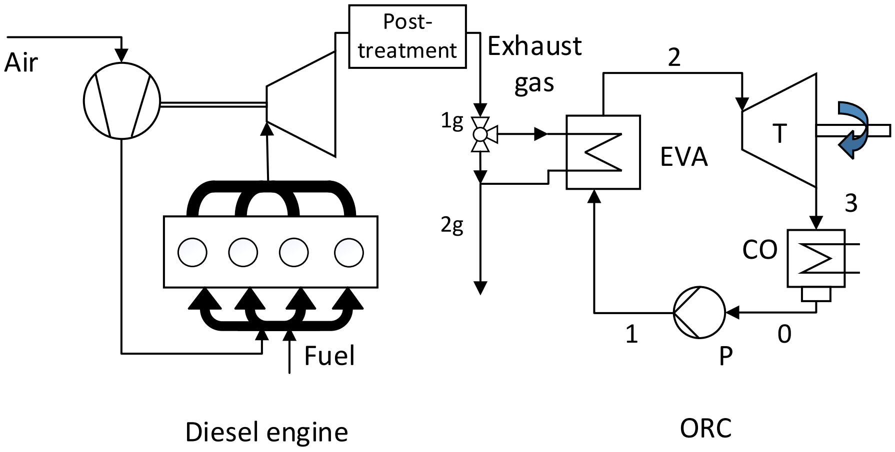

Fig. 1. Basic layout of the ORC waste heat recovery system.

2.2. Waste heat profile

The exhaust gas data used in this work were provided by a truck manufacturer and consist of measurements of a 450-hp (331 kW) 13-L turbocharged diesel engine over a 45-min trip of a heavy-duty truck; see Fig. 2. The exhaust data are provided as supplementary material in Appendix B. The data sampling time is 1 s.

The fluctuations in temperature, shown in Fig. 2a, are dampened by the engine post-treatment system (selective catalytic reactor), and oscillate over a 65 K range between 270 °C and 335 °C. On the contrary, the fluctuations in mass flow rate are highly transient, fluctuating between 0.05 kg/s and 0.52 kg/s and showing rapid variations from maximum to minimum and vice versa in the time scale of only a few seconds.

From the mass flow rate $\dot{m}_g$ in kg/s and inlet temperature $T_{g,in}$ in K of the exhaust gas, the available waste heat rate $\dot{Q}_{g,a}$ can be determined as follows:

$$\dot{Q}_{g,a} = \dot{m}_g c_{p,g} \left(T_{g,in} - 120 - 273.15\right) \tag{1}$$

where $c_{p,g}$ is the specific heat at constant pressure of the exhaust gas. The waste heat rate is referred here to an outlet temperature of the exhaust gas of 120 °C in order to avoid condensation of acidic substances in the tailpipe. It can be seen in Fig. 2b that the available waste heat is affected by large variability, fluctuating between 8 kW and 96 kW. Furthermore, the large variability of the available waste heat is confirmed by its profile load curve plotted in Fig. 3. It can be seen that the distribution of the available waste heat rate is approximately uniform. This causes particular challenges to the design of the ORC unit and leads to part-load operation for most of the time during the profile. Based on industry experience, the exhaust gas heat rate data corresponding to 51.5 kW was selected as the design point for the ORC unit. This approximately corresponds to the average available waste heat rate over the profile in Fig. 2, and it is indicated with a red star in Fig. 3.

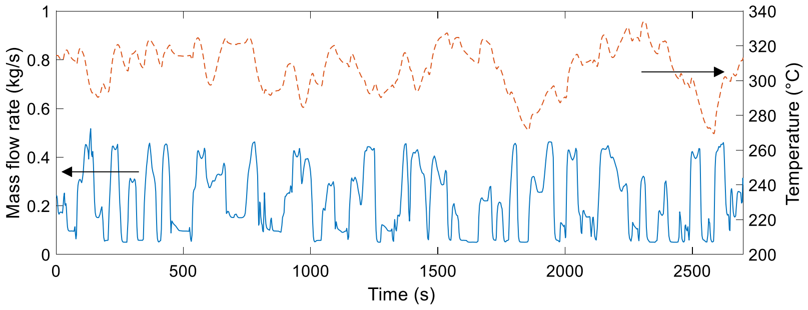

(a)

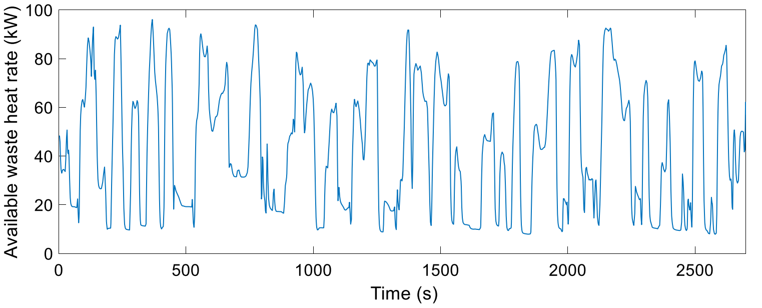

(b)

Fig. 2. (a) Exhaust gas mass flow rate and inlet temperature and (b) available waste heat rate.

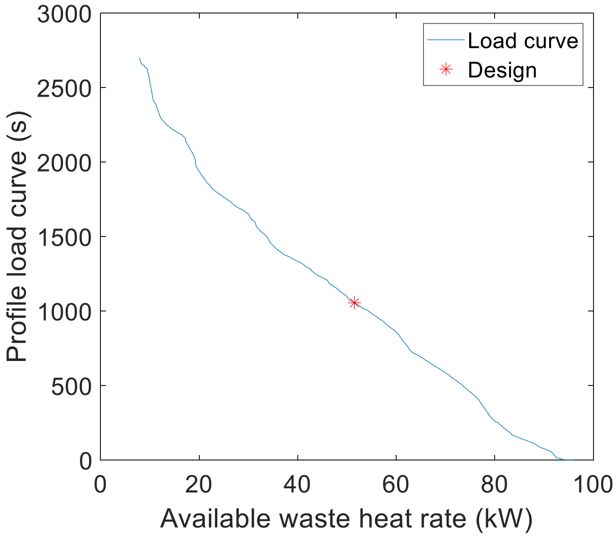

Fig. 3. Available waste heat rate of a 450-hp (331 kW) 13-L turbocharged diesel engine over a 45-min trip of a heavy-duty truck (assuming 120 °C as the reference temperature).

2.3. Design of the ORC system and evaporator

The ORC system was designed by carrying out a steady-state thermodynamic cycle optimization of the system depicted in Fig. 1. Details about the design can be found in Ref. (Carraro et al., 2021). The system design conditions are reported in Table 1. Water was assumed as the cooling medium, entering the condenser at 40 °C. The ORC working fluid is R245fa, analogously to that used in Ref. (Peralez et al., 2017). R245fa is selected as working fluid due to its high thermal degradation temperature of 300 °C and its low flammability, which is a significant benefit compared with hydrocarbons and siloxanes (highly flammable). The objective function to be maximized by the optimization routine is the net power output P_{net}:

$$P_{net} = \dot{m}_{wf}\ \left(h_{wf,T,in} - h_{wf,T,out}\right) + \dot{m}_{wf}\ \left(h_{wf,P,in} - h_{wf,P,out}\right) \tag{2}$$

where $\dot{m}_{wf}$ and h_{wf} are the mass flow rate and the specific enthalpy of the working fluid, respectively, and the subscripts ‘T’ and ‘P’ refer to the turbine and the pump, respectively. The subscripts ‘in’ and ‘out’ refer to the inlet and the outlet of the component..

After the thermodynamic design, the evaporator was designed using an in-house design code written in MATLAB®. The code was originally developed in Refs (Pili et al., 2017). and also used in Ref. (Carraro et al., 2021). A fin-and-tube evaporator is considered, where the exhaust gas flows on the shell side and the working fluid on the tube side in a crossflow arrangement. This type of heat exchanger is suitable for this application, because it can guarantee compactness while limiting the backpressure of the main diesel engine and being easy to clean in the case of fouling. These advantages are achieved thanks to the larger flow channels on the exhaust gas side compared with, e.g., plate heat exchangers. The tubes are equipped with radial fins to enhance the heat transfer. The evaporator design is illustrated in Fig. 4, and the main geometrical parameters of the evaporator are summarized in Table 2. Stainless steel is chosen as the material to avoid corrosion from the exhaust gas acidic compounds.

Table 1
Design parameters of the ORC unit (Carraro et al., 2021).

Fluid	Quantity	Symbol	Unit	Value
Exhaust gas	Mass flow rate	$\dot{m}_g$	kg/s	0.25
Exhaust gas	Inlet temperature	$T_{g,in}$	°C	320
Exhaust gas	Outlet temperature	$T_{g,out}$	°C	120
Working fluid	Mass flow rate	$\dot{m}_{wf}$	kg/s	0.187
Working fluid	Inlet temperature	$T_{wf,in}$	°C	56
Working fluid	Outlet temperature	$T_{wf,out}$	°C	171
Working fluid	Evaporation pressure	$p_{wf,EVA}$	bar	29.0
Working fluid	Condensing pressure	$p_{wf,CO}$	bar	4.2
Working fluid	Turbine isentropic efficiency	$\eta_{is,T,D}$	%	85
Working fluid	Pump isentropic efficiency	$\eta_{is,P,D}$	%	75
Working fluid	Net mechanical power output	P_{net}	kW	6.2

3. Dynamic modeling of the organic Rankine cycle system

In this section, the modeling approaches used to simulate the ORC system and to develop the feedforward control concepts are described. Focus is set on the high-pressure part of the ORC unit consisting of the working fluid pump, the evaporator and the turbine. For simplicity, given its minor relevance, the condenser of the ORC unit is neglected. In particular, the evaporator is of central interest, since this component thermally connects the ORC unit with the heat source and is, therefore, an essential element for guaranteeing the maximum power output. Here, two models are illustrated: i) the finite volume model, which is typically more accurate and therefore used to simulate the real ORC system on which the control strategies are tested and ii) the moving boundary model, which is less computationally-intensive and therefore can be used to develop advanced control strategies, such as nonlinear feedforward.

3.1. Finite volume evaporator model

A dynamic model of the ORC evaporator was developed by using the commercial software Dymola and the commercial library TIL (hermo GmbSuit, 2016). Given its proven superior accuracy, a FV approach was used to simulate the real ORC system, whereas a moving boundary approach was used for the controller development; see section 3.2. The simulation model and the control system were integrated into the Simulink® environment, where the Dymola model was imported by using the Functional Mock-up Interface through the FMI Kit for Simulink (Systèmes, 2018). Given the high number of tube rows, the FV evaporator was modelled as a parallel flow heat exchanger. 1D discretization was performed by using 15 cells, distributed along the main ORC working fluid direction.

The mass and energy balances for each cell of the working fluid are as follows:

$$\frac{dM_{wf}}{dt} = \frac{d\left(V_{wf}\ \rho_{wf}\right)}{dt} = V_{wf}\left(\left.\frac{\partial\rho_{wf}}{\partial h}\right|_{p}\frac{dh_{wf}}{dt} + \left.\frac{\partial\rho_{wf}}{\partial p}\right|_{h}\frac{dp_{Wf}}{dt}\right) = \dot{m}_{wf,in} - \dot{m}_{wf,out} \tag{3}$$

$$\frac{d\left(M_{wf}\ u_{wf}\right)}{dt} = \frac{d\left(M_{wf}\ h_{wf} - V_{wf}p_{wf}\right)}{dt} = \dot{m}_{wf,in}h_{wf,in} - \dot{m}_{wf,out}\ h_{wf,out} + \dot{Q}_{cell,wf} \tag{4}$$

where M is the mass, V is the volume, ρ is the density, h is the specific enthalpy, p is the pressure, $\dot{m}$ is the mass flow rate, u is the specific internal energy and $\dot{Q}_{cell}$ is the heat transfer rate of the working fluid. The subscripts ‘in’ and ‘out’ refer to the inlet and the outlet of the cell, and the subscript ‘wf’ refers to the working fluid. The TIL library uses an upwind discretization scheme, according to which the specific enthalpy

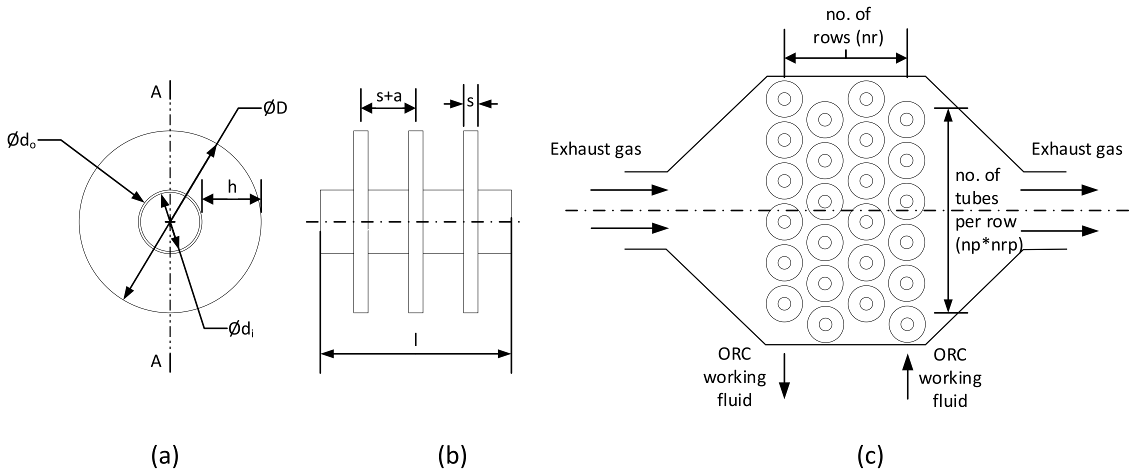

Fig. 4. Geometry of the fin-and-tube evaporator: (a) tube and fin cross section, (b) tube axial view and (c) fluid arrangement (Carraro et al., 2021).

Table 2
Main geometrical parameters of the fin-and-tube evaporator (Carraro et al., 2021).

Quantity	Symbol	Unit	Value
Tube inner diameter	d_i	mm	12.4
Tube thickness	t	mm	1.1
Tube length	l	mm	388.8
Tube spacing between rows	t_{n_r}	mm	29.1
Tube spacing between tubes in same row	t_{n_p}	mm	34.1
Fin height	h	mm	5.4
Fin thickness	s	mm	0.5
Fin pitch	a	mm	3.3
Number of tube rows	n_r	–	17
Number of tube per row	$n_p{\cdot}n_{rp}$	–	8
Number of passes per row (tube side)	n_{rp}	–	2
Tube arrangement	–	–	Staggered
Tube and fin material	–	–	Stainless steel

of the cell is assumed equal to the specific enthalpy of the fluid at the cell outlet, i.e. $h_{wf,out} = h_{wf}$. The pressure drop was neglected here for simplicity, which is known to be a reasonable assumption for dynamic simulations. The energy balance for the metallic wall of the heat exchanger is as follows:

$$M_w c_w \frac{dT_w}{dt} = -\dot{Q}_{cell,wf} + \dot{Q}_{cell,g} \tag{5}$$

where M_w, c_w and T_w are the mass, specific heat and temperature of the wall, respectively. $\dot{Q}_{cell,g}$ is the heat transfer rate between the exhaust gas and the ORC working fluid. Since the dynamics of the exhaust gas are much faster than those of the metallic wall and the working fluid, the cells of the exhaust gas were modelled at steady state as follows:

$$\dot{m}_{g,out} = \dot{m}_{g,in} \tag{6}$$

$$\dot{Q}_{cell,g} = \dot{m}_{g,in} c_{p,g} \left(T_{g,in} - T_{g,out}\right) \tag{7}$$

where $c_{p,g}$ is the gas specific heat at constant pressure. The pressure drop was neglected also here for simplicity, which is known to be a reasonable assumption for dynamic simulations. The heat transfer rates at the working fluid and the gas side implemented in the TIL library were used here as follows (hermo GmbSuit, 2016):

$$\dot{Q}_{cell,wf} = \frac{1}{\frac{1}{\alpha_{wf} A_i} + \frac{R_w}{2}} \left(T_w - T_{wf}\right) \tag{8}$$

$$\dot{Q}_{cell,g} = \dot{m}_{g,in} c_{p,g} \left(1 - \exp\left\{ - \frac{1}{\left[\frac{1}{\alpha_g A_o \left(1 + \frac{A_f}{A_o}\left(\eta_f - 1\right)\right)} + \frac{R_w}{2}\right] \dot{m}_{g,in} c_{p,g}} \right\}\right) \left(T_{g,in} - T_w\right) \tag{9}$$

where α_{wf} and α_g are the heat transfer coefficients on the working fluid and on the gaseous heat source side, A_i and A_o the respective heat transfer surface areas, R_w the thermal resistance of the metallic wall, A_f the heat transfer area of the fins and η_f the fin efficiency. The exponential term of the heat transfer rate of the gas takes into account that the exhaust gas locally flows in crossflow with respect to the tubes. The Gnielinski-Dittus-Boelter correlation (Pili et al., 2019a) was used for the heat transfer coefficient α_{wf} of the working fluid in single phase, while the Steiner correlation from the VDI Heat Atlas (Kind et al., 2010) was used for the two-phase region. For the exhaust gas, the correlation for heat transfer on the shell-side of tube bundles from the VDI Heat Atlas (Gaddis and Gnielinski, 2010) was used. The fin efficiency was determined by using the method suggested by Schmidt (1945). The working fluid properties were retrieved using the REFPROP database (Lemmon et al., 2018), while the XTR dry air model of the TILMedia library (hermo GmbMedia, 2016) was used to model the properties of the exhaust gas.

In the FV method, the cells of the working fluid do not necessarily have a unique fluid phase (liquid, two-phase or vapor). This can vary depending on the operating conditions and the heat transfer rate. However, the phase transition in a cell can lead to numerical problems in the solution, because of the large difference in the heat transfer coefficient α_{wf} and the fluid density ρ_{wf} between the liquid, two-phase and vapor. For this reason, a time filter with a time constant $T_{\alpha_{wf}} = 1$ s was included in the α_{wf} calculation. This allows for a smoother phase change as follows:

$$\frac{d\alpha'_{wf}}{dt} = \frac{\alpha_{wf} - \alpha'_{wf}}{T_{\alpha_{wf}}} \tag{10}$$

where the filtered heat transfer coefficient α'_{wf} was used in Eq. (8)

instead of α_{wf} as the latter is determined by the heat transfer correlations for single and two-phase flow introduced before.

In ORC power systems, the system response due to dynamic changes in operating conditions is governed by the heat exchangers. This is because the thermal transients have much larger time constants than the mechanical transients. For this reason, the dynamics of the fluid machinery, i.e. the turbine and the pump, are neglected, and these components are modelled at steady state. When making this assumption, no significant loss of accuracy in the prediction of the dynamic trend for the system thermodynamic properties is expected (Imran et al., 2020). In addition, the turbine is assumed to operate at sonic condition, since this is typically the case for ORC applications (Macchi and Astolfi, 2017). Therefore, the following equation holds:

$$\dot{m}_{wf,T}\frac{\sqrt{\kappa_{wf,T,in}\,Z_{wf,T,in}\,T_{wf,T,in}}}{p_{wf,T,in}}=k_T \tag{11}$$

whereκ is the ratio of the specific heats, and Z is the compressibility factor for the working fluid at the turbine inlet. The parameter $k_T = 0.128\frac{kg}{s}\frac{K^{0.5}}{kPa}$ was estimated from the design values of mass flow rate, pressure and temperature at the turbine inlet. The isentropic efficiency of the turbine at part-load is defined by the correlation from Vetter (2014):

$$\frac{\eta_{is,T}}{\eta_{is,T,D}}=0.007+3.182\left(\frac{\dot{m}_{wf,T}}{\dot{m}_{wf,T,D}}\right)-6.491\left(\frac{\dot{m}_{wf,T}}{\dot{m}_{wf,T,D}}\right)^2+10.504\left(\frac{\dot{m}_{wf,T}}{\dot{m}_{wf,T,D}}\right)^3-11.413\left(\frac{\dot{m}_{wf,T}}{\dot{m}_{wf,T,D}}\right)^4+7.068\left(\frac{\dot{m}_{wf,T}}{\dot{m}_{wf,T,D}}\right)^5-1.856\left(\frac{\dot{m}_{wf,T}}{\dot{m}_{wf,T,D}}\right)^6 \tag{12}$$

where the subscript ‘D’ refers to the design point previously described in section 2. A positive-displacement pump was considered, and its part-load performance was estimated as a function of the pressure ratio of the pump p_r as follows (Pili et al., 2019b):

$$\eta_{is,P,v}\left(\frac{p_r}{p_{r,D}}\right)=\eta_{is,P,D}\left(0.992\,e^{-0.01529\frac{p_r}{p_{r,D}}}-0.6902\,e^{-6.82\frac{p_r}{p_{r,D}}}\right)\eta_{is,P}=\eta_{is,P,D}\frac{\eta_{is,P,v}\left(\frac{p_r}{p_{r,D}}\right)}{\eta_{is,P,v}\left(\frac{p_r}{p_{r,D}}=1\right)} \tag{13}$$

3.2. Moving boundary evaporator model

The FV model presented in the previous section consists of 46 states, i.e. the specific enthalpies and the filter heat transfer coefficients of the working fluid cells, the pressure of the working fluid as well as the wall temperatures of the metallic wall cells. The high number of states of the FV model leads to a high computational effort, which is generally undesirable for real-time control. For this reason, while the FV model was used in this work only to simulate the real system, a MB model was used for the development of the feedforward control. The model was implemented in Simulink®, which allows for flexible model modifications and easy development of innovative control concepts, such as the nonlinear dynamic inversed-model feedforward presented in this work.

The MB model consists of three cells, corresponding to the liquid, two and vapor phase of the working fluid, respectively. During operation, the interface between each phase region can move depending on the operating conditions and the local heat transfer rate. The mass balance in each cell is as follows:

$$\frac{dM_{wf}}{dt}=\frac{d\left(V_{wf,tot}\,y_{wf}\,\rho_{wf}\right)}{dt}=V_{wf,tot}\left[\rho_{wf}\,\frac{dy_{wf}}{dt}+y_{wf}\left(\left.\frac{\partial\rho_{wf}}{\partial h}\right|_p\frac{dh_{wf}}{dt}+\left.\frac{\partial\rho_{wf}}{\partial p}\right|_h\frac{dp_{Wf}}{dt}\right)\right]=\dot{m}_{wf,in}-\dot{m}_{wf,out} \tag{14}$$

where y_{wf} corresponds to the volume fraction of the cell with respect to the total volume $V_{wf,tot}$. The energy balance for each cell is

$$\frac{d(H_{wf})}{dt}-V_{wf,tot}\,y_{wf}\frac{dp_{wf}}{dt}=\dot{m}_{wf,in}\,h_{wf,in}-\dot{m}_{wf,out}\,h_{wf,out}+\dot{Q}_{cell,wf} \tag{15}$$

where $H_{wf}=M_{wf}h_{wf}$ is the enthalpy of the working fluid in the cell. The specific enthalpy of each cell was calculated, analogously to the correspondent TIL library model, as the average of the specific enthalpy at its inlet and outlet:

$$h_{wf}=\frac{h_{wf,in}+\,h_{wf,out}}{2} \tag{16}$$

The density and the enthalpy in the two-phase region are defined by the void fraction γ_{wf}, corresponding to the ratio of the volume occupied by the vapor phase to the total volume:

$$\rho_{wf}=\rho_{wf}^{'}\left(1-\gamma_{wf}\right)+\rho_{wf}^{''}\,\gamma_{wf} \tag{17}$$

$$H_{wf}=\left[\rho_{wf}^{'}h_{wf}^{'}\left(1-\gamma_{wf}\right)+\rho_{wf}^{''}\,h_{wf}^{''}\,\gamma_{wf}\right]y_{wf}V_{wf,tot} \tag{18}$$

where $\rho^{'}$ and ρ'' are the densities of the saturated liquid and vapor, respectively. Analogously, $h^{'}$ and h'' are the specific enthalpies of the saturated liquid and vapor. The void fraction γ_{wf} was determined by using the correlation from Zivi (1964).

The energy balance at the metallic wall accounts for the variation of the volume in each cell, being a modified version of Eq. (5):

$$\frac{d\left(V_{w,tot}\,\rho_w\,y_w\,c_w\,T_w\right)}{dt}=\sum\frac{d\left(V_{w,tot}\,\rho_w\,c_w\,y_w\right)}{dt}T_{w,b}-\dot{Q}_{cell,wf}+\dot{Q}_{cell,g} \tag{19}$$

where $V_{w,tot}$ is the total volume of metallic wall material, ρ_w is the density of the metallic wall material, y_w is the volume fraction of the considered region and $T_{w,b}$ is the temperature of the neighboring region

Table 3
Exponential factors for the estimation of the heat transfer coefficients.

Fluid	Phase	Quantity	Symbol	Unit	Value
Exhaust gas	–	Design heat transfer coefficient	$\alpha_{g,D}$	W/m^{2}K	66.4
		Design mass flow rate	$\dot{m}_{g,D}$	kg/s	0.25
		Exponential factor	$\tau_{g,D}$	–	0.54
Working fluid	Liquid, L	Design heat transfer coefficient	$\alpha_{wf,L,D}$	W/m^{2}K	770
		Design mass flow rate	$\dot{m}_{wf,L,D}$	kg/s	0.187
		Exponential factor	$\tau_{wf,L}$	–	0.92
	Two-phase, LV	Design heat transfer coefficient	$\alpha_{wf,LV,D}$	W/m^{2}K	1550
		Design mass flow rate	$\dot{m}_{wf,LV,D}$	kg/s	0.187
		Exponential factor	$\tau_{wf,LV}$	–	0.67
	Vapor, V	Design heat transfer coefficient	$\alpha_{wf,V,D}$	W/m^{2}K	1000
		Design mass flow rate	$\dot{m}_{wf,V,D}$	kg/s	0.187
		Exponential factor	$\tau_{wf,V}$	–	0.86

of working fluid, which changes according to the direction of change of the interface boundary:

$$T_{w,b} = \begin{cases} T_w \ if \dfrac{dy_w}{dt} < 0 \\ T_{w,n} \ elsewhere \end{cases} \tag{20}$$

where $T_{w,n}$ is the wall temperature of the neighboring cell. The mass and energy balance equations for the gas cell are the same as in Eqs. (6) and (7). In order to simplify the calculation of the heat transfer coefficients in off-design conditions, the correlations were fitted by using an exponential function of the mass flow rate, similarly to what was carried out for the global heat transfer coefficient in Ref. (Pili et al., 2019b):

$$\alpha = \alpha_D \left(\frac{\dot{m}}{\dot{m}_D}\right)^{\tau} \tag{21}$$

where τ is an exponential factor. The heat transfer coefficients and the exponential factors used for the working fluid and the exhaust gas in each region are summarized in Table 3. The need of fins to enhance the heat transfer on the evaporator shell side is confirmed by the low heat transfer coefficient of the exhaust gas compared with the working fluid. In addition, it can be seen that the two-phase region shows the highest heat transfer coefficient for the working fluid. Untypically, the heat transfer coefficient of the working fluid is higher in the vapor region compared with the liquid region. This is due to the much larger velocity of the working fluid given by the lower density for the same available cross section in this region compared with the liquid region. Nonetheless, the much lower heat transfer coefficient of the exhaust gas dominates the heat transfer capabilities of the heat exchanger and makes the differences in heat transfer coefficient of the working fluid in the different regions negligible. Section 3.3 shows the suitability of the fitting when estimating the part-load behavior of the evaporator on a test case. The REFPROP database was used to retrieve the properties of the working fluid, whereas the specific heat at constant pressure of the exhaust gas was approximated by a polynomial function:

$$c_p\left(T_g\right) = 2.19 \cdot 10^{-4}\, T_g^2 - 4.40 \cdot 10^{-2}\, T_g + 9.99 \cdot 10^2 \tag{22}$$

where T_g is defined in K. By combining the mass and energy balances described by Eqs. (14) and (15), it can be concluded that the MB model has 8 states, i.e. the specific enthalpy of the working fluid at inlet and outlet of the evaporator, the pressure, the volume fraction of the liquid and vapor regions with respect to the total volume and the temperature of the metallic wall in the three regions. The number of states is significantly lower than that of the FV model, allowing for faster and more sophisticated control.

3.3. Verification of evaporator models and model reduction

In the absence of suitable experimental data, the Simulink® models were verified against the results of models in different software, such Aspen Exchanger Design and Rating (EDR) (Aspen Technology, 2017) and Dymola. The heat transfer coefficients of the evaporator are the largest element of uncertainty and largely affect the heat transfer area and the off-design behavior of the evaporator. Since the heat transfer correlations are static, a steady-state verification was first performed by varying the mass flow rate of the exhaust gas and working fluid over a broad range of operating conditions (25%–100% of the design mass flow rates). As the baseline, a simulation of the evaporator in Aspen EDR was used. The geometric parameters.

presented in Table 2 and the exponential factors shown in Table 3 were used. The results are presented in Fig. 5a, indicating that both the Dymola FV model and the Simulink® MB model are very close to the reference case in Aspen EDR, with a maximum deviation of 2%.

A dynamic verification was also performed among the Dymola FV and MB models and the Simulink® MB model, by starting from nominal conditions and subjecting the evaporator to a positive step of 20% in pump mass flow rate at $t = 500$ s; see Fig. 5b. In this case, the FV and MB models of the TIL library are compared with the MB model developed in Simulink®. The step in pump mass flow rate causes the degree of

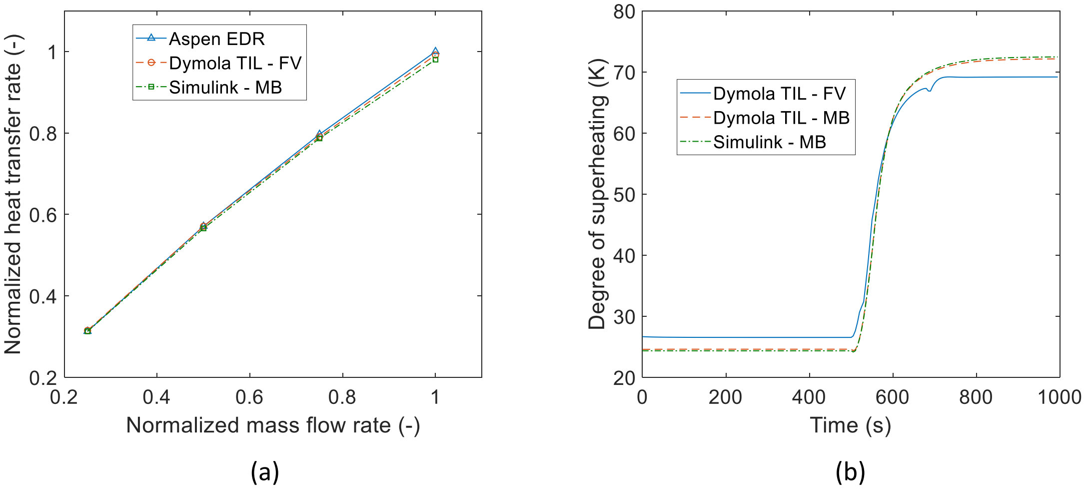

Fig. 5. Verification of evaporator models: (a) steady state simulations and (b) dynamic simulations of a 20% step change in the pump mass flow rate.

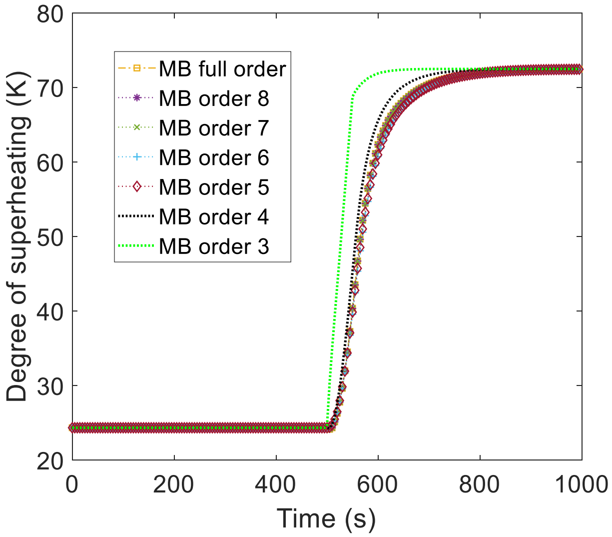

Fig. 6. Dynamic response of reduced-order MB models over a 20% step change in pump mass flow rate.

superheating to increase by more than 40 K. The FV model has a small fluctuation at $t = 700$ s, which is caused by a cell that switched from liquid to two-phase. This phenomenon is typical of FV models and well documented in literature (Desideri et al., 2016). Also the response of the MB model available from the TIL library in Dymola is shown. The differences in results between the MB model from Dymola and the MB Simulink® model are negligible. Both MB models have an offset in the degree of superheating compared with the FV model, although this remains below 5 K before and after the step change. The responses of the evaporator to the step change are very similar for the FV and MB evaporator models, with slightly more time required by the MB model to reach its steady state, because of the higher degree of superheating reached after the transient. Overall, the good agreement among the results of the models indicates that the models are reasonable and reliable.

Not all the states of the MB evaporator model have the same dynamic time scale. Some of them, e.g., the pressure, is significantly faster, while others, e.g., the wall temperatures, are considerably slower. Since the overall system dynamics are governed by the slowest states, the MB model can be reduced by neglecting the dynamic effect of the faster states, i.e. setting their time derivatives to zero. This should lead to only small deviations from the full-order original model. A comparison of the reduced-order models is carried out based on the 20% step change in pump mass flow rate previously used for the verification of the Simulink® MB model, and the response is plotted in Fig. 6. Table 4 shows the states that are neglected and the corresponding model order. In addition, the time required to reach 63.2% of the final steady-state value is given. This time value corresponds to the time constant of first-order linear systems (Corriou, 2004), and is used here for comparison. The full MB model has a time constant of 58.6 s. It can be.

seen that the models with order five to seven do not show significant deviation from the full MB model – the models with order five and six have time constants deviating less than 2 s from that of the full-order model, while the model with order seven has the same time constant as the full-order model. This means that the specific enthalpies at the evaporator inlet and outlet and the evaporation pressure have much faster dynamics than the other states. By neglecting the volume fraction of the vapor region, the time constant drops to about 51 s. A much more significant drop occurs by neglecting the time derivative of the liquid region, since the time constant is reduced to 23 s and the evaporator response becomes noticeably faster. In particular, the volume fraction of the liquid region has a greater influence on the dynamics than the volume fraction of the vapor region, because of the much larger density and hence larger mass of working fluid included in the liquid phase.

Table 4
Order reduction of MB model.

Order	Time derivative set to zero	Symbol	Time constant to reach 63.2% of final steady-state value, s
8 (Full)	-	-	58.6
7	Specific enthalpy at inlet	$h_{wf,in}$	58.6
6	Pressure	p_{wf}	60.8
5	Specific enthalpy at outlet	$h_{wf,out}$	60.1
4	Volume fraction (length) of vapor region	$y_{w,V}$	50.8
3	Volume fraction (length) of liquid region	$y_{wf,L}$	23.0

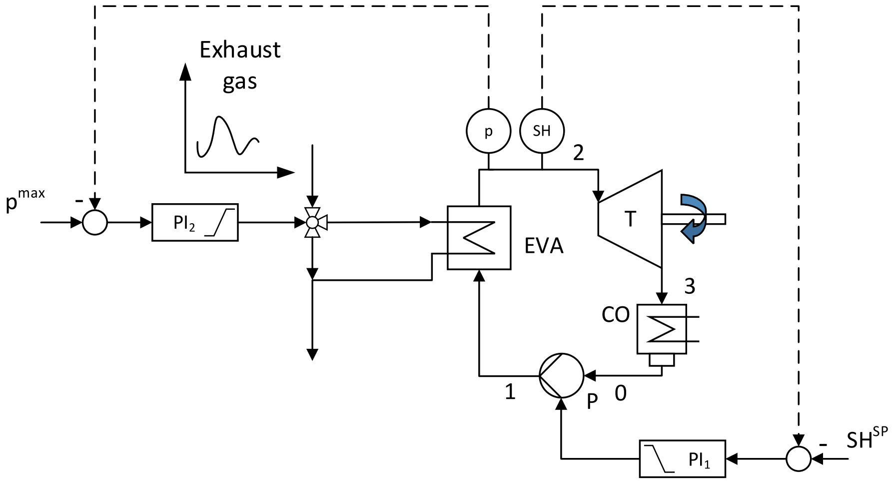

Fig. 7. Feedback control structure with PI control.

4. Control of the organic Rankine cycle system

In this section, the reference PI control of the ORC system is first discussed, with focus on the control of the working fluid conditions at the evaporator outlet/turbine inlet. Subsequently, the static, linear and nonlinear inversed-model feedforward concepts are presented.

4.1. Basic feedback control structure

The basic PI control structure for the waste heat recovery ORC unit is the one illustrated in Fig. 7. Emphasis is set on the working fluid conditions at the turbine inlet (point 2), because these conditions are the most affected by the exhaust gas conditions and influence the mechanical power output of the turbine. Important constraints need to be satisfied at this point, such as the minimum degree of superheating and the maximum evaporation pressure. These conditions are required in order to ensure optimal and safe operation. For this purpose, two PI controllers were considered:

1) A main controller with the task to keep the degree of superheating at point 2 at its desired set point SH^{SP} by acting on the pump mass flow rate $\dot{m}_{wf,P}$;
2) A secondary controller with the task to ensure that the pressure at point 2 does not exceed the maximum allowed value p^{max}, which is set to 35 bar to avoid supercritical operation. In order to fulfill this task, a share of the exhaust gas can be bypassed the evaporator reducing the heat transfer rate of the evaporator.

Both controllers are equipped with output limiters to ensure the practical feasibility of the solution and to avoid component damage. The operational range of the pump is constrained to a range of 20%–120% of its nominal value (Pili et al., 2019a), while the opening of the bypass valve may vary from completely closed (0) to completely open (1). An anti-windup system is included in the PI controllers to avoid accumulation of the integral part when the controller is either at the maximum or at the minimum value (Corriou, 2004).

The PI controllers were designed by using the ‘pidtune’ command available from the Controller System Toolbox™ of MATLAB® (Mathworks®, 2019), based on the linearization of the system around the design point. The parameters were tuned with a standard phase margin of 60°. The values for the proportional and integral gain of the PI controller are reported in Table 5. In addition, the PI tuning proposed in Ref (Skogestad, 2004). and available in the Control System Designer App of MATLAB® (MathWorks®, 2019) was used for comparison; see Table 5. It can be seen that the proportional gain for the pump controller is much higher, and the integral time constant is lower using the method presented in Ref (Skogestad, 2004). than those obtained using the ‘pidtune’ command, leading to a much more aggressive controller using the method presented in Ref. (Skogestad, 2004) (see section 5). For the bypass controller, a pure proportional controller was obtained using the ‘pidtune’ command, while a PI controller with a lower proportional gain was obtained using the method presented in Ref. (Skogestad, 2004).

In the simple feedback configuration of Fig. 7, the measurements of mass flow rate $\dot{m}_g$ and inlet temperature $T_{g,in}$ of the exhaust gas are not directly given as information to the controllers, but they rather act as disturbances that affect the degree of superheating and the evaporation pressure. The PI controllers can counteract the influence of the disturbances; however, they can only act after the detection of the disturbances at point 2.

A similar approach can be followed for the temperature and pressure of the working fluid at the condenser outlet (point 0), which correspond to the conditions at the pump inlet and can be considered as disturbances for the control system in Fig. 7. Furthermore, it is common practice for ORC systems to control the condenser pressure by varying the mass flow rate of the cooling fluid. If no control is available, the heat transfer rate and pressure in the condenser are dependent only on the truck incoming air flow rate during a driving cycle, which in turn is directly related to the vehicle speed. Considerations of the condenser conditions require a specific analysis of the low-pressure part of the ORC unit, including the heat rejection capabilities of the system to the environment. In order to reduce the problem complexity, and given the slow variations affecting the operating conditions at the condenser compared to the fast variations in waste heat, considerations of the condenser conditions are discarded in the present work, as previously done in Ref. (Seitz et al., 2018). The condenser pressure is assumed to stay constant at the design value of 4.2 bar.

4.2. Feedforward control

This section describes the different feedforward concepts analyzed in this work, starting from the static feedforward concept, followed by the gain-scheduled linear feedforward concept and leading to the nonlinear dynamic inversed-model feedforward concept. Novel approximations to allow for the implementation of nonlinear dynamic inversed-model feedforward are described at the end of the section.

4.2.1. Static feedforward

Considering the turbine off-design law defined by Eq. (11) and assuming that the mass flow rate of the pump corresponds to the mass flow rate at the turbine inlet, a direct correlation is found between the mass flow rate of the pump and the desired degree of superheating:

$$\dot{m}_{wf,P} \cong \dot{m}_{wf,T} = k_T \cdot \frac{p_{wf,T,in}}{\sqrt{\kappa_{wf,T,in}\left(SH^{SP},\ p_{wf,T,in}\right) Z_{wf,T,in}\left(SH^{SP},\ p_{wf,T,in}\right) \left[T_{wf,sat,T,in}\left(p_{wf,T,in}\right) + SH^{SP}\right]}} \tag{23}$$

where $p_{wf,T,in} = p_{wf,EVA}$ is the pressure measured at the turbine inlet and $T_{wf,sat,T,in}\left(p_{wf,T,in}\right)$ is the saturation temperature of the fluid at the turbine inlet pressure. The main drawback of this concept lies in the fact that the time delay between the mass flow rate of the pump and that of the turbine is neglected, although it has a significant influence on the system

Table 5
Tuning of PI controllers.

Controlled variable	Manipulated variable	Method	Proportional gain	Integral time constant
Degree of superheating at turbine inlet	Mass flow rate of pump	pidtune	−0.0011 K/kg/s	7.35 s
Degree of superheating at turbine inlet	Mass flow rate of pump	Ref. (Skogestad, 2004)	−0.0284 K/kg/s	4.04 s
Maximum evaporation pressure	Bypass opening	pidtune	−0.0036 1/kPa	–
Maximum evaporation pressure	Bypass opening	Ref. (Skogestad, 2004)	−0.0021 1/kPa	–

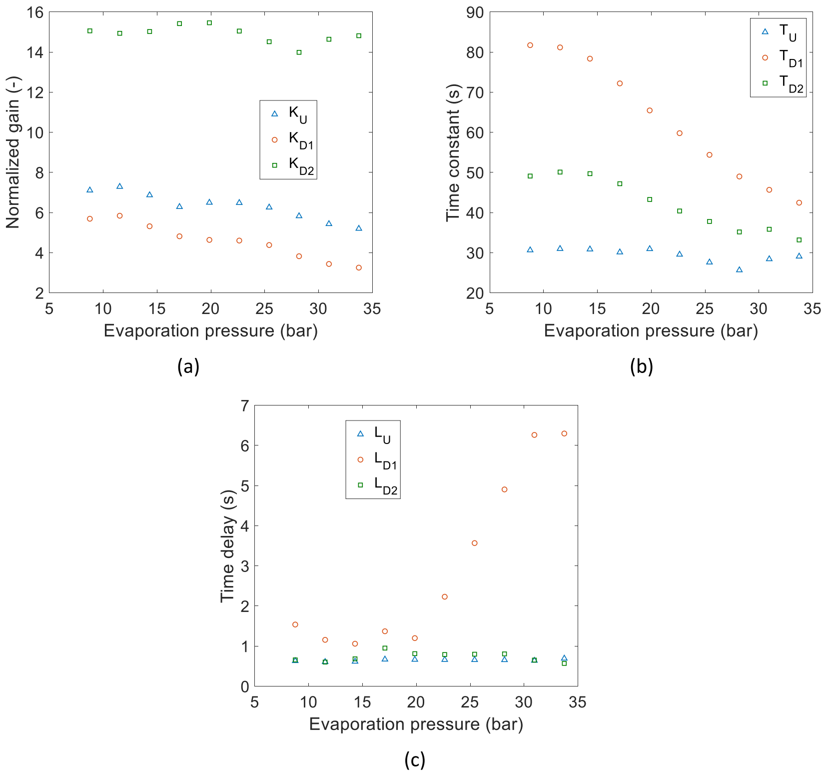

(a)

(b)

(c)

Fig. 8. System identification for the ORC evaporator dynamic response: (a) normalized gain, (b) time constant and (c) time delays for the identified response of the ORC system. Identification on a 1% step change in input 'U' and disturbances 'D1' and 'D2'.

dynamic response.v

4.2.2. *Gain-scheduled linear dynamic inversed-model feedforward*

A model of the high-pressure part of the ORC unit can be inverted to find the value of mass flow rate of the pump that ensures the desired set point. The development of the inversed-model feedforward control can be simplified by approximating the ORC model as a first-order plus dead time (FOPDT) system, i.e. in the Laplace domain:

$$SH_{wf,T,in}(s) = \frac{K_U}{1+T_U s} e^{-L_U\ s} \dot{M}_{wf,P}(s) \tag{24}$$

where K_U is the system gain, T_U a time constant, L_U the time delay resulting from the dead time, and $SH_{wf,T,in}(s)$ and $\dot{M}_{wf,P}(s)$ are the Laplace transform of the actual degree of superheating at turbine inlet and mass flow rate of the pump, respectively. The system gain K_U, the time constant T_U and the time delay L_U are found by using the system identification method suggested in Ref. (Astrom and Hagglund, 2009). The degree of superheating stays at the desired set point only if the model perfectly matches the real system. If this is not the case, a deviation of the actual operating point from the desired set point will occur. The dynamic behavior of the ORC evaporator is highly nonlinear, and according to Refs. (Feru et al., 2014; Seitz et al., 2018) the approximation in Eq. (24) is not able to predict the system behavior with sufficient accuracy over a broad operating range. For this reason, the model is developed for several operating points, so that the system in Eq. (24) can be tuned as a function of a proper scheduling parameter θ:

$$SH_{wf,T,in}(s) = \frac{K_U(\theta)}{1+T_U(\theta)s} e^{-L_U(\theta)s} \dot{M}_{wf,P}(s) \tag{25}$$

The same can be done to estimate the variation of degree of superheating when the system is exposed to variations in mass flow rate $\dot{M}_g(s)$ and inlet temperature $T_{g,in}(s)$ of the exhaust gas:

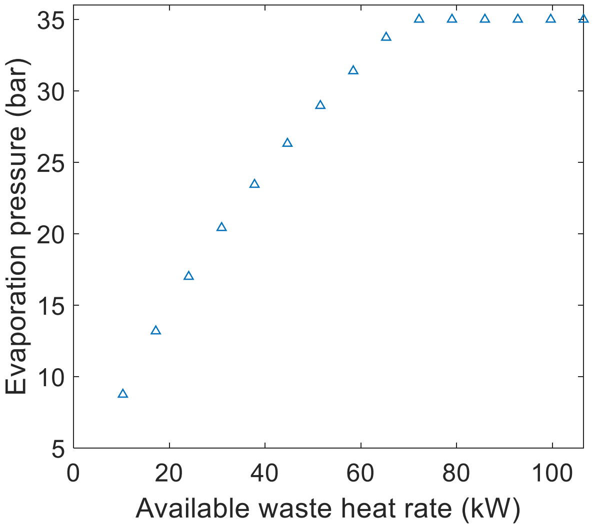

Fig. 9. Evaporation pressure as a function of the available waste heat (assuming 120 °C as the reference temperature).

$$SH_{wf,T,in}(s) = \frac{K_{D1}(\theta)}{1+T_{D1}(\theta)s} e^{-L_{D1}(\theta)s} \dot{M}_g(s) \tag{26}$$

$$SH_{wf,T,in}(s) = \frac{K_{D2}(\theta)}{1+T_{D2}(\theta)s} e^{-L_{D2}(\theta)s} T_{g,in}(s) \tag{27}$$

where the subscript 'D1' (disturbance 1) refers to the mass flow rate and the subscript 'D2' (disturbance 2) refers to the inlet temperature of the

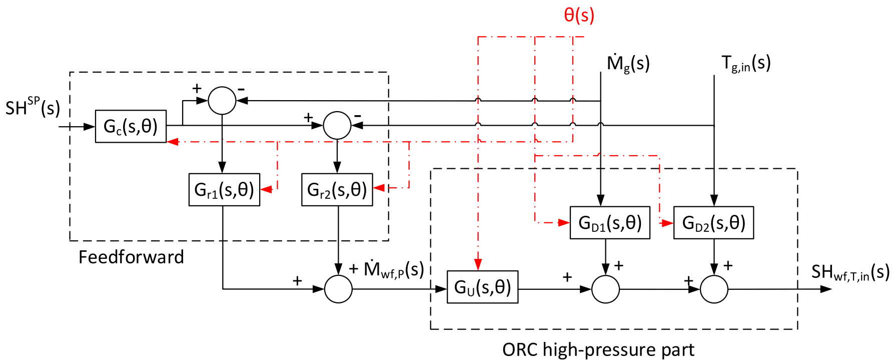

Fig. 10. Linear dynamic inversed-model feedforward concept for the high pressure part of the ORC unit as a function of the scheduling parameter θ. The concept has been presented in (Corriou, 2004).

exhaust gas. The coefficients are illustrated as a function of the evaporation pressure in Fig. 8, which is taken in this case as the scheduling parameter θ. The maximum scheduling pressure is limited to 35 bar, because this is the maximum allowed for the system under investigation. The relative root mean square error of the identified models compared with the original FV models is 3.2%. Linear interpolation is used during the simulations to estimate the parameters between consecutive identified systems. It can be seen that the normalized gains K_U and K_{D1} (normalized with respect to the steady-state input and output) drop with increasing evaporation pressure, whereas K_{D2} oscillates around the values 14–16 (Fig. 8a). The time constants T_U, T_{D1} and T_{D2} also drop with increasing evaporation pressure, as shown in Fig. 8b, although T_U remains relatively close to 30 s. The identified time delay is plotted in Fig. 8c. While L_U and L_{D1} are below 1 s and are relatively independent from the pressure, L_{D2} is between 1 and 2 s for low pressures, but grows up to 6.5 s for evaporation pressures above 30 bar.

The large variability of the gains, time constants and time delays over the pressure range confirms the nonlinearity of the evaporator model and the need for parameter scheduling. Therefore, in addition to the evaporation pressure, the available waste heat rate $\dot{Q}_{g,a}$ defined in Eq. (1) was used as an alternative scheduling parameter (Koppauer et al., 2018). Fig. 9 shows that the evaporation pressure increases with increasing available waste heat rate. The increase in pressure is limited to 35 bar as previously mentioned. Results for the cases of the evaporation pressure and the available waste heat rate used as scheduling parameters are presented for the linear dynamic inversed-model feedforward concept in section 5.

Once the coefficients of the FOPTD models are identified, the total variation of the degree of superheating can be found by adding all the single contributions in Eqs. (25)-27):

$$SH_{wf,T,in}(s) = G_U(s,\theta)\,\dot{M}_{wf,P}(s) + G_{D1}(s,\theta)\,\dot{M}_g(s) + G_{D2}(s,\theta)\,T_{g,in}(s) \tag{28}$$

with $G_U(s,\ \theta)\ =\ \frac{K_U(\theta)}{1+T_U(\theta)s}e^{-L_U(\theta)s}$, $G_{D1}(s,\theta)\ =\ \frac{K_{D1}(\theta)}{1+T_{D1}(\theta)s}e^{-L_{D1}(\theta)s}$ and $G_{D2}(s,\theta)\ =\ \frac{K_{D2}(\theta)}{1+T_{D2}(\theta)s}e^{-L_{D2}(\theta)s}$ the transfer functions for the mass flow rate of the pump as well as the heat source parameters of the mass flow rate and inlet temperature, respectively.

Given the desired set point $SH^{SP}(s)$, the mass flow rate of the pump can be determined by inverting Eq. (28) as follows:

$$\dot{M}_{wf,P}(s) = \frac{1}{G_U(s,\theta)}SH^{SP}(s)\ - \frac{G_{D1}(s,\theta)}{G_U(s,\theta)}\ \dot{M}_g(s) - \frac{G_{D2}(s,\theta)}{G_U(s,\theta)}\ T_{g,in}(s) \tag{29}$$

The feedforward concept proposed in (Corriou, 2004) and shown in Fig. 10 is used to calculate the mass flow rate of the pump by

$$\begin{aligned}\dot{M}_{wf,P}(s) = {} & [G_{r1}(s,\theta) + G_{r2}(s,\theta)]\ G_c(s,\theta)\ SH^{SP}(s)\ \ - G_{r1}(s,\theta)\ \dot{M}_g(s) \\ & - G_{r2}(s,\theta)\ T_{g,in}(s)\end{aligned} \tag{30}$$

By comparing Eq. (29) and Eq. (30), the transfer functions $G_{r1}(s,\theta)$, $G_{r2}(s,\theta)$ and $G_c(s,\theta)$ are found (the notation is consistent with that used in Ref (Corriou, 2004).):

$$G_{r1}(s,\theta) = \frac{G_{D1}(s,\theta)}{G_U(s,\theta)} \tag{31}$$

$$G_{r2}(s,\theta) = \frac{G_{D2}(s,\theta)}{G_U(s,\theta)} \tag{32}$$

$$G_c(s,\theta) = \frac{1}{G_U(s,\theta)[G_{r1}(s,\theta) + G_{r2}(s,\theta)]} = \frac{1}{G_{D1}(s,\theta) + G_{D2}(s,\theta)} \tag{33}$$

In order to ensure feasibility of the feedforward options, it has to be assured that the transfer functions $G_{r1}(s,\theta)$, $G_{r2}(s,\theta)$ and $G_C(s,\theta)$ have a degree of the denominator higher or equal to the degree of the numerator. For this reason, a time filter with time constant $T_f = 0.1\,s$ is included in $G_c(s,\theta)$, and the delays $L_{D1}(\theta)$ and $L_{D2}(\theta)$ are neglected. In case of $L_{D1}(\theta) < L_U(\theta)$ or $L_{D2}(\theta) < L_U(\theta)$, the time delay is set to zero in $G_{r1}(s,\theta)$ and $G_{r2}(s,\theta)$, so that the resulting time delay is always positive and the transfer function is causal and therefore feasible.

4.2.3. Nonlinear dynamic inversed-model feedforward

The MB model expressed in section 3.2 can be expressed in a compact

Table 6
Approximations for inversed full-order and reduced-order MB models.

Order	Approximations
8 (Full)/ 7	• $\frac{dy_1}{dt} = 0$ in the energy balance for working fluid in the two-phase cell ('LV') • $\frac{dM_3}{dt} = 0$ in the energy balance for working fluid in the vapor cell ('V') • Filter on the outlet specific enthalpy with $\tau_h\ = 0.4\ s$: $\frac{dh_{wf,out}}{dt} = \frac{h(SH^{SP},\ p_{wf}) - h_{wf,out}}{\tau_h}$
6	• Energy balance for the working fluid in the two-phase cell ('LV') at steady state $0\ =\ \dot{m}_{wf,LV,in}h^{'}_{wf} - \dot{m}_{wf,LV,out}h^{''}_{wf} + \dot{Q}_{LV,wf}$ • Energy balance for the working fluid in the vapor cell ('V') at steady state $0\ =\ \dot{m}_{wf,V,in}h^{''}_{wf} - \dot{m}_{wf,out}h_{wf,out} + \dot{Q}_{V,wf}$ • Filter on the outlet specific enthalpy with $\tau_h\ = 0.4\ s$: $\frac{dh_{wf,out}}{dt} = \frac{h(SH^{SP},\ p_{wf}) - h_{wf,out}}{\tau_h}$
5	• Energy balance for the working fluid in the two-phase cell ('LV') at steady stat $0\ =\ \dot{m}_{wf,LV,in}h^{'}_{wf} - \dot{m}_{wf,LV,out}h^{''}_{wf} + \dot{Q}_{LV,wf}$ • Energy balance for the working fluid in the vapor cell ('V') at steady state $0\ =\ \dot{m}_{wf,V,in}h^{''}_{wf} - \dot{m}_{wf,out}h_{wf,out} + \dot{Q}_{V,wf}$
4	• Energy balance for the working fluid in the two-phase cell ('LV') at steady state $0\ =\ \dot{m}_{wf,LV,in}h^{'}_{wf} - \dot{m}_{wf,LV,out}h^{''}_{wf} + \dot{Q}_{LV,wf}$
3	No approximation required: minimum phase system

form as follows:

$$\dot{x} = f(x, u, d) \quad y = g(x, u, d) \tag{34}$$

where x is the state vector, u is the input vector, d is the disturbance vector, y is the output vector, f is the state function and g is the output function. Given a desired set point of the output y^{SP}, the nonlinear dynamic inversed-model feedforward control law is defined as follows:

$$u^{FFW} = g^{-1}\left(x, y^{SP}, d\right) \tag{35}$$

where u^{FFW} is the vector of the ideal manipulated variables given by the feedforward control. It can be seen that the feedforward law requires knowledge of the system state x, the desired set point y^{SP} and the disturbance d. If some of these quantities are not known or measurable, they need to be estimated. As state estimators for nonlinear systems, an Extended Kalman Filter (EKF) can be used analogously to the approach presented in Refs. (Rathod et al., 2019; Koppauer et al., 2018; Peralez et al., 2017). As an alternative, the Unscented Kalman Filter (UKF) was adopted.

in Ref. (Pili et al., 2020b). Even though the EKF is more commonly used, the EKF and UKF showed comparable computational effort (Kandepu et al., 2008). The feedforward control requires also an inversion of the output function g, which is only possible for minimum phase systems, i.e. systems whose inverse and themselves are causal and stable. The full-order MB model and the reduced-order models, except the third-order model, are not minimum phase (also called non-minimum phase). That is, an inversed-model feedforward concept cannot be developed unless the original model description (described by Eq. (34)) is modified. An example of approximation for a linear non-minimum phase system is briefly explained in Appendix A.

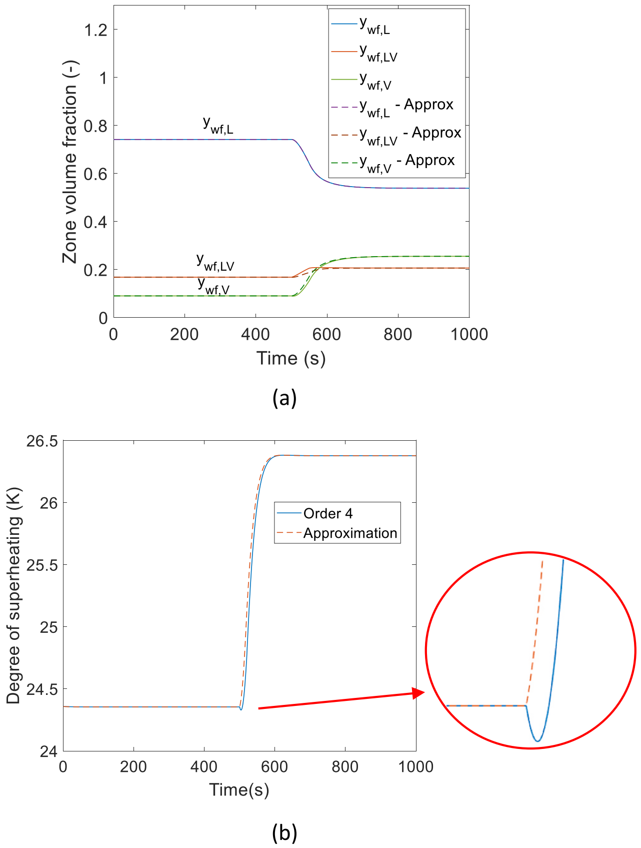

Fig. 11. Approximation of the fourth-order MB model subjected to 1% step change in the pump mass flow rate: (a) volume fraction of each phase region and (b) degree of superheating.

4.2.4. *Approximations for nonlinear dynamic inversed-model feedforward concepts*

The nonlinear full-order and reduced-order MB models, compared in section 3.3, can be approximated in a way that the inversed-models are causal and stable and can thus be used for feedforward control. The approximations made for each model order are reported in Table 6. In general, the approximations for models of order four to six assume steady state energy balances in the two-phase and vapor regions. For the models of order seven and eight, where the time derivative of the pressure is different from zero, the inversed system can be stabilized by setting $\frac{dy_1}{dt} = 0$ in the energy balance of the two-phase region and $\frac{dM_3}{dt} = 0$ in the energy balance of the vapor region. Although the approximations are the same, the models of order seven still differs from the eight-order model because the model of order seven neglects the time derivative of the specific enthalpy of the working fluid at inlet, i.e. $\frac{dh_{wf,in}}{dt} = 0$.

Additionally, the derivative of the specific enthalpy at the evaporator outlet in the inversed models of order five to eight is determined by using a time filter, which accounts for variations of the set point SH^{SP} and evaporation pressure. The time constant $\tau_h = 0.4$ s was found to ensure sufficient stability of the ORC system with the feedforward concept.

The approximations in the two-phase and vapor energy balances reduce the time delay caused by the mass accumulation terms in the two-phase and vapor regions. Fig. 11 shows the impact of the time delay on the cell density ρ_{wf} and volume fraction y_{wf}. The time delay is responsible for the initial inversed response of the degree of superheating at the evaporator outlet. The fourth-order system is subjected to a 1% negative step change in the pump mass flow rate.

In this system, the vapor region is completely at steady state, whereas the mass and energy balances of the two-phase regions are

$$-V_{wf,tot}\left[(1-\gamma)\rho_{wf}^{'} + \gamma\rho_{wf}^{''}\right]\frac{dy_{wf,L}}{dt} = \dot{m}_{wf,LV,in} - \dot{m}_{wf,out} \tag{36}$$

$$-V_{wf,tot}\left[(1-\gamma)\rho_{wf}^{'}h_{wf}^{'} + \gamma\rho_{wf}^{''}h_{wf}^{''}\right]\frac{dy_{wf,L}}{dt} = \dot{m}_{wf,LV,in}h_{wf}^{'} - \dot{m}_{wf,out}h_{wf}^{''} + \dot{Q}_{LV,wf} \tag{37}$$

The approximated energy balance is

$$0 = \dot{m}_{wf,LV,in}h_{wf}^{'} - \dot{m}_{wf,out}h_{wf}^{''} + \dot{Q}_{LV,wf} \tag{38a}$$

The effect of the approximation can be described as follows (see Fig. 11a). First, the negative step in mass flow rate leads to a reduction of the volume fraction of the liquid zone $y_{wf,L}$, in order to satisfy the mass and energy balance in this region (Eqs. (14) and (15)). This leads in turn to an initial increase in the mass flow rate moving from the liquid to the two-phase region and thus to mass accumulation in the two-phase region. This causes a steep initial increase of the volume fraction of the two-phase region $y_{wf,LV}$. The satisfaction of the energy balance in the two-phase region causes the initial increase in the two-phase region to be larger than the decrease in the liquid region, resulting in an initial decrease of the volume fraction of the vapor region $y_{wf,V}$ and in the total heat exchanger volume remaining constant. Consequently, the degree of superheating at the evaporator outlet also decreases. However, after the initial transient, the reduction in mass flow rate of the pump causes the working fluid to require less volume fraction $y_{wf,LV}$ to be fully evaporated. As a result, the vapor volume fraction $y_{wf,V}$ increases, and so does the degree of superheating at the evaporator outlet. It can be seen in Fig. 11b that by neglecting the mass accumulation in the two-phase energy balance, the initial inversed response of the original model (although small) disappears.

5. Comparison of control concepts

The feedback and feedforward concepts described in section 4 are compared. In particular, the following cases are investigated:

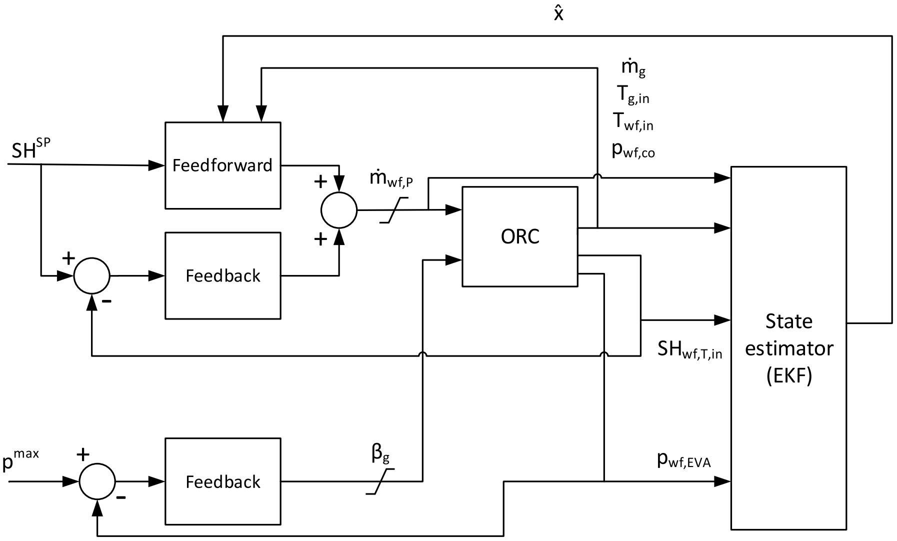

Fig. 12. General scheme of the feedforward and feedback control concepts.

- only feedback (PI) using ‘pidtune’;
- only feedback (PI) using the tuning rules from Ref. (Skogestad, 2004);
- feedback using ‘pidtune’ and linear dynamic inversed-model feedforward using the evaporation pressure as the scheduling parameter;
- feedback using ‘pidtune’ and linear dynamic inversed-model feedforward using the available waste heat rate as the scheduling parameter;
- feedback using ‘pidtune’ and nonlinear dynamic inversed-model feedforward from order three to eight, with the Extended Kalman Filter (EKF, see section 4.2.3) for state estimation (sample time equal to 0.5 s).

A basic general control scheme is presented in Fig. 12. The mass flow rate of the pump $\dot{m}_{wf,P}$ is controlled to achieve the desired set point in degree of superheating SH^{SP}. The controller acting on the pump consists of a feedforward and a feedback part. The feedback part has been described in section 4.1. The feedforward can be based on the static, gain-scheduled linear or the nonlinear concepts presented in section 4.2. The static and gain-scheduled linear feedforward are based on algebraic and transfer functions, respectively, and do not need any state estimation. If a nonlinear feedforward is included, this.

requires the estimation $\hat{x}$ of the system state x. This is done by using an EKF, based on the MB model of the correspondent order of the feedforward model. The EKF uses the evaporation pressure $p_{wf,EVA}$ and the temperature of the working fluid at evaporator outlet (derived by the degree of superheating at turbine inlet $SH_{wf,T,in}$ and the evaporation pressure $p_{wf,EVA}$) as measurements (system outputs) for the state estimation. In addition, the mass flow rate of the pump $\dot{m}_{wf,P}$ and the disturbances are given as input to the EKF. As mentioned in section 4.1, a second feedback controller limits the maximum pressure of 35 bar by acting on the bypass opening of the exhaust gas β_g to avoid excessive pressure and keep the operation in the subcritical region.

The analysis of the controller performance focuses mainly on the pump controller, given the fact that the bypass controller has the only objective of limiting the maximum pressure of the ORC evaporator. In order to compare the pump controller performance, two main variables are considered, namely, the absolute root mean square tracking error (ARMSTE) and the cumulative controller effort Qu:

$$ARMSTE=\sqrt{\frac{1}{t_f}\int_0^{t_f}\left(SH_{wf,T,\ in}-SH^{SP}\right)^2dt} \qquad (38)\text{b}$$

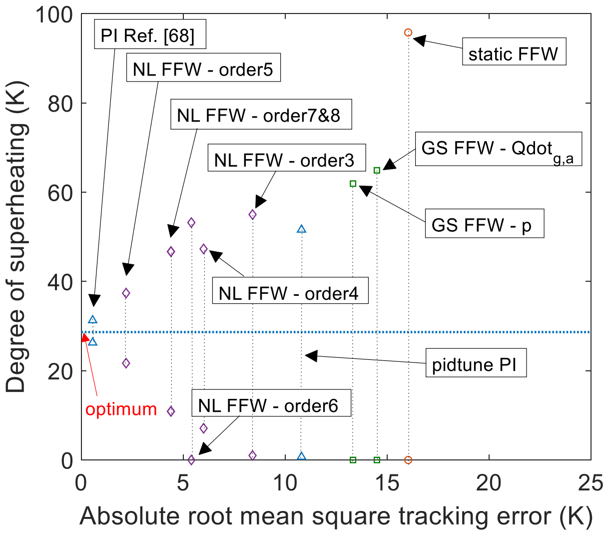

Fig. 13. Maximum and minimum degree of superheating for different control concepts. Legend: ‘pidtune PI’ = PI feedback with MATLAB® pidtune command, ‘PI Ref (Skogestad, 2004). = PI feedback with tuning rule from Ref (Skogestad, 2004).’, ‘static FFW’ = static feedforward, ‘GS FFW’ = linear dynamic inversed-model feedforward with gain-scheduling, ‘NL FFW’ = nonlinear dynamic inversed-model feedforward.

$$Qu=\frac{1}{t_f}\frac{1}{\left|\dot{m}_{wf,P,\ max}-\dot{m}_{wf,P,\ min}\right|}\int_0^{t_f}\left|\frac{d\dot{m}_{wf,P}}{dt}\right|dt \qquad (39)$$

where $t_f = 45$ min is the profile time duration and $\dot{m}_{wf,P,\ max}$ and $\dot{m}_{wf,P,\ min}$ are the maximum and minimum mass flow rates of the pump, respectively. The ARMSTE is a measure of the average absolute deviation of the degree of superheating from the desired set point. Given the fact that the set point is kept constant during the entire driving cycle while the waste heat varies rapidly and acts as a disturbance, in this work the ARMSTE measures the controller performance in terms of disturbance rejection. For the controller to have good disturbance rejection capability, the ARMSTE should be as low as possible. Q_u is a measure of the average absolute time variation of the mass flow rate of the pump, normalized with respect to the possible variation range. The higher the Q_u, the more aggressive and oscillatory the controller action and vice versa. However, in order to extend the lifetime of the ORC pump, it is desirable to achieve the smoothest operation possible. For this reason, the Q_u should also be as low as possible. Other important quantities for the comparison are the minimum and the maximum degree of superheating. In particular, the degree of superheating should always be positive to avoid liquid droplets at the turbine inlet, because droplets could damage this component.

5.1. Results

Fig. 13 presents a comparison of the different control alternatives by illustrating the maximum and the minimum degree of superheating as a function of the ARMSTE. At this point, only the ability of the control system to keep the degree of superheating close to the set point is evaluated, and no considerations are made about how severe the controller action acts on the ORC pump. The set point is marked in Fig. 13 by a solid horizontal line. The closer the maximum and minimum degree of superheating are to the set point line, the better can the controller reject the waste heat disturbances. It can be seen that there is a correlation between the ARMSTE and the maximum and minimum degree of superheating over the profile. The points where the ARMSTE is the lowest result in the maximum and minimum degrees of superheating being closer to the set point of 28.9 K and vice versa. The 'pidtune' feedback PI controller shows an ARMSTE of 10.8 K, and a minimum degree of superheating of 0.7 K. Therefore, the risk of liquid droplets at the turbine inlet with this controller is high. The feedback PI tuned using the tuning rules presented in Ref. (Skogestad, 2004), instead, outperforms all other feedback/feedforward concepts in terms of ARMSTE, keeping the degree of superheating very close to the set point, with fluctuations only between 26.3 K and 31.3 K. The feedforward ('static FFW') and the linear dynamic inversed-model feedforward ('GS FFW') cannot ensure a positive degree of superheating over the entire heat source profile. This is mainly because they are not able to predict the dynamics of the ORC unit with sufficient accuracy. For this reason, they are not applicable solutions. The result is that they even worsen the already insufficient performance of the 'pidtune' PI feedback controller. On the contrary, the nonlinear dynamic inversed-model feedforward options ('NL FFW') are able to reduce the ARMSTE with respect to the 'pidtune' feedback PI and guarantee a positive degree of superheating. An exception is caused by the sixth-order NL FFW model that, despite the low ARMSTE, is affected by a large fluctuation in the degree of superheating at $t = 1600$ s, which leads to liquid droplets at the turbine

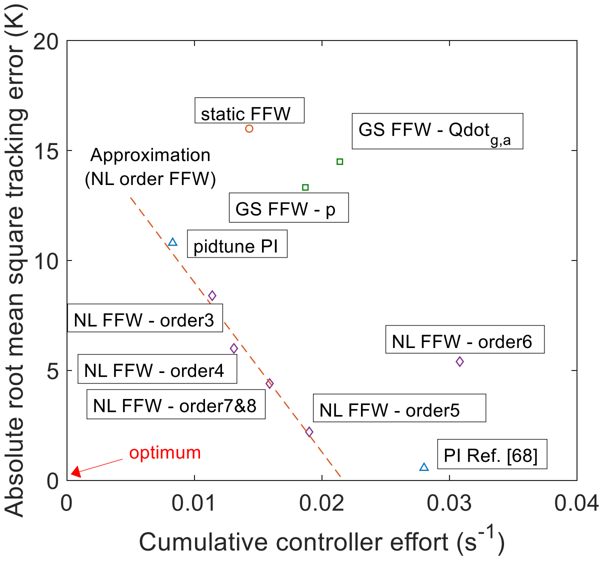

Fig. 15. Controller performance: absolute mean square tracking error as a function of the cumulative controller effort. 'pidtune PI' = PI feedback with MATLAB® pidtune command, 'PI Ref (Skogestad, 2004). = PI feedback with tuning rule from Ref (Skogestad, 2004).', 'static FFW' = static feedforward, 'GS FFW' = linear dynamic inversed-model feedforward with gain-scheduling, 'NL FFW' = nonlinear dynamic inversed-model feedforward.

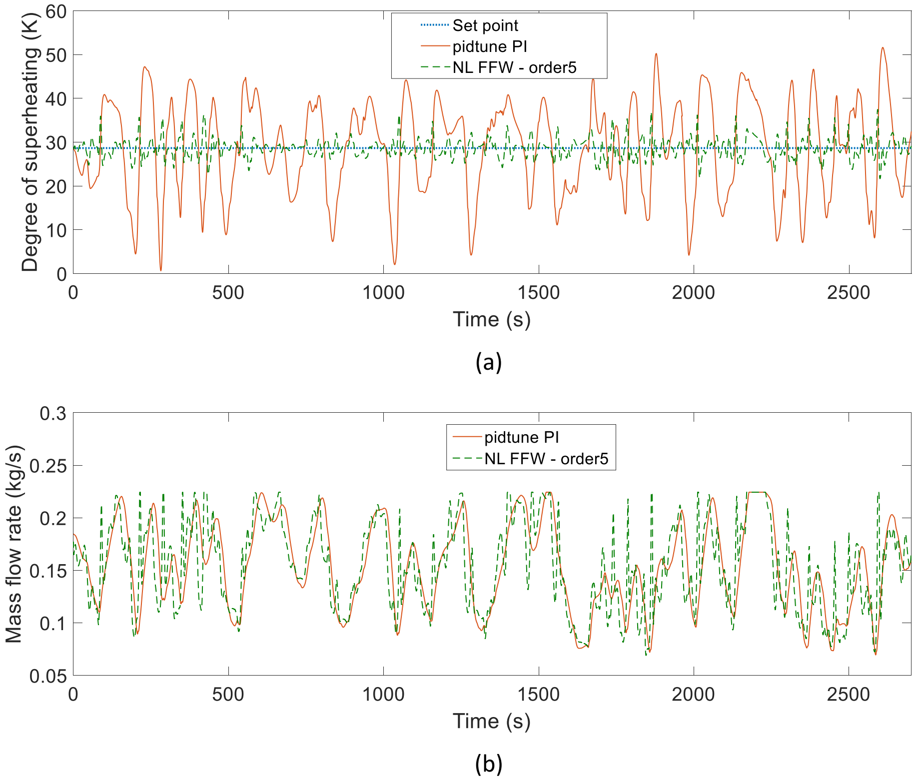

Fig. 14. Controller performance: (a) disturbance rejection on degree of superheating and (b) mass flow rate of the pump.

inlet for approximately 10 s. For this reason, the spread between the maximum and minimum degrees of superheating is larger in this case. Among the NL FFW solutions, the fifth-order model shows the lowest ARMSTE at 2.2 K, and the smallest fluctuations in the degree of superheating between 21.7 K and 37.4 K.

Considering the results of Fig. 6, a similar dynamic response of the degree of superheating should be expected among the NL FFW models of order higher than four. However, the ARMSTE of the fifth-order NL FFW model is lower than the ARMSTE of the models of higher order. The reason for this is the difference in the time derivative of the specific enthalpy at the evaporator outlet, which is directly related to the degree of superheating. In fact, differently from the fifth-order NL FFW model, the specific enthalpy at the evaporator outlet is a state in the models of order from six to eight, and its time derivative is determined by using a first-order filter (see Table 6). The filter, which is necessary to ensure the feasibility of the feedforward concept, includes a fictitious lag to the thermodynamic conditions at turbine inlet and thus worsens the dynamic prediction capabilities of the feedforward concept. As a result, the control performance in terms of disturbance rejection degrades for models of order higher than five, in contrast to the considerable improvement that is achieved when increasing the model order from three to five.

A comparison of the 'pidtune' feedback case and the fifth-order NL FFW case over time is illustrated in Fig. 14. This comparison can show the benefits of including the feedforward scheme to a classical PI feedback scheme. The time behavior of the degree of superheating is plotted in Fig. 14a. The results show that the 'pidtune' feedback controller is not able to keep the degree of superheating close to the set point, which oscillates in the range ±30 K from the set point. On four occasions, the degree of superheating drops below 5 K, showing high risk of liquid droplets at the turbine inlet. The integration of the fifth-order NL FFW to the same classical PI controller can, on the other hand, considerably reduce the oscillations in the degree of superheating to ±7 K from the set point, with the minimum degree of superheating more than 20 K away from the critical operating range for the turbine. However, as shown in Fig. 14b, the mass flow rate of the pump changes much faster in the fifth-order system to adapt the mass flow rate of the working fluid to the quick variations of the mass flow rate of the exhaust gas. This causes higher mechanical and thermal stresses on the ORC pump and its drive.

In order to account for both the disturbance rejection capabilities and the stresses on the system actuator, an overview of the performance of the different control solutions is presented in Fig. 15. The cumulative controller effort, linked to the component stresses, is shown on the abscissa, and the ARMSTE, representative of the disturbance rejection capabilities, is shown on the ordinate. The results indicate that the 'pidtune' feedback PI controller, although showing high ARMSTE, reaches the lowest cumulative controller effort at 0.8%/s. On the other hand, the remarkably good disturbance rejection capabilities of the tuning rules of Ref (Skogestad, 2004). described previously are achieved with a significantly higher Q_u of 2.8%/s, which indicates that the controller is relatively aggressive and changes the mass flow rate quite rapidly (the Q_u value is 3.5 times higher than that of the 'pidtune' feedback controller). The very high Q_u might strongly affect the feasibility of the feedback PI controller based on the tuning rules of Ref. (Skogestad, 2004), because of the lifetime reduction induced by the rapid actuator changes imposed by the controller. For instance, the electric motor driving the pump could fail because of the excessive torque demand required by very rapid accelerations in rotational speed. For this reason, a better trade-off between the ARMSTE and Q_u is desirable.

Fig. 15 highlights the advantages of using a nonlinear model to develop an inversed-model feedforward compared to the feedback controllers and the other FFW options. The NL FFW is able to reduce the ARMSTE with respect to the 'pidtune' feedback controller, by keeping a moderate Q_u. The dashed straight line in Fig. 15 highlights the trade-off between disturbance rejection performance (low ARMSTE) and long lifetime of the pump (low Q_u). All NL FFW cases except for the sixth-order model lie in the proximity of the dashed straight line. The NL FFW third-order model, which is minimum phase and does not require any approximation, is able to achieve an ARMSTE of 8.4 K and a Q_u of 1.1%/s. The fifth-order model provides the lowest ARMSTE among the NL FFW solutions at 2.2 K, but higher Q_u at 1.9%/s.

Both the static FFW and the GS FFW lead to neither a lower ARMSTE nor a lower Q_u with respect to the 'pidtune' feedback and the NL FFW cases, and therefore they are not beneficial. The static FFW leads to a higher ARMSTE and cumulative controller effort compared with the 'pidtune' PI case, and does not lead therefore to any advantage. The same occurs for the GS FFW which can only outperform the static FFW. The case of the evaporation pressure performs better as the scheduling parameter than the available waste heat rate, with lower cumulative controller effort at 1.87%/s compared to 2.14%/s, and lower ARMSTE at 13.3 K compared with 14.5 K.

5.2. Discussion and comparison to previous works

The results discussed so far can be compared with the third-order nonlinear inversed-model feedforward suggested in Ref. (Peralez et al., 2017), which achieved outstanding performance in rejecting the fluctuations of waste heat. The model presented in Ref (Peralez et al., 2017). differs from the third-order NL FFW case illustrated in this work, because a multivariable approach was used based on the assumption of a two-time-scale dynamic behavior between the degree of superheating and the pressure control. In that case, the superheating control was assumed to be much faster than the pressure control and, consequently, the state observer (still based on an EKF estimator) and the pressure controller (which acted on the exhaust gas bypass opening) were developed considering the degree of superheating equal to its set point. In this way, only the pressure is considered as the suitable input measurement for the EKF, while the temperature of the working fluid at the evaporator outlet can be found by the evaporation pressure and the set point in the degree of superheating. This assumption allowed for the development of a relatively simple, implicit continuous-time EKF state observer and a nonlinear feedback controller for the control of the evaporation pressure by acting on the exhaust gas bypass valve. Another important difference between the controller presented in Ref (Peralez et al., 2017). and the third-order NL FFW suggested in this work is the flow arrangement for the exhaust gas, which is in crossflow in Ref (Peralez et al., 2017). and in parallel flow in the third-order NL FFW case. However, the crossflow arrangement leads to relatively large deviations for heat exchangers with a high number of tube rows. For example, the TIL library (hermo GmbSuit, 2016) suggests to use the parallel flow arrangement for a number of tube rows higher than three, and it was therefore preferred for the evaporator considered in this work, which has 17 tube rows. Other sources of uncertainty are the controller and the EKF parameters used in Ref. (Peralez et al., 2017), whose values are not explicitly stated in the original research, nor are any other numerical details on the original heat exchanger geometry and setup available. For the comparison, the proportional constant $k = 0.5\,kPa^{-1}$ and the same covariance matrices as in the third-order NL FFW case are used.

The time response of the degree of superheating is compared with the third-order and fifth-order NL FFW models in Fig. 16a. It can be seen that the degree of superheating oscillates more frequently and with a higher amplitude in the case of Ref (Peralez et al., 2017). compared with the other NL FFW models. The time behavior of the mass flow rate of the pump is shown in Fig. 16b. The fluctuations are less abrupt for the approach presented in Ref. (Peralez et al., 2017), followed by the third-order NL FFW case. The fifth-order NL FFW model has the fastest variations in mass flow rate of the pump and can thus achieve a better disturbance rejection performance. Correspondingly, the cumulative controller effort Q_u for the model in Ref (Peralez et al., 2017). was close

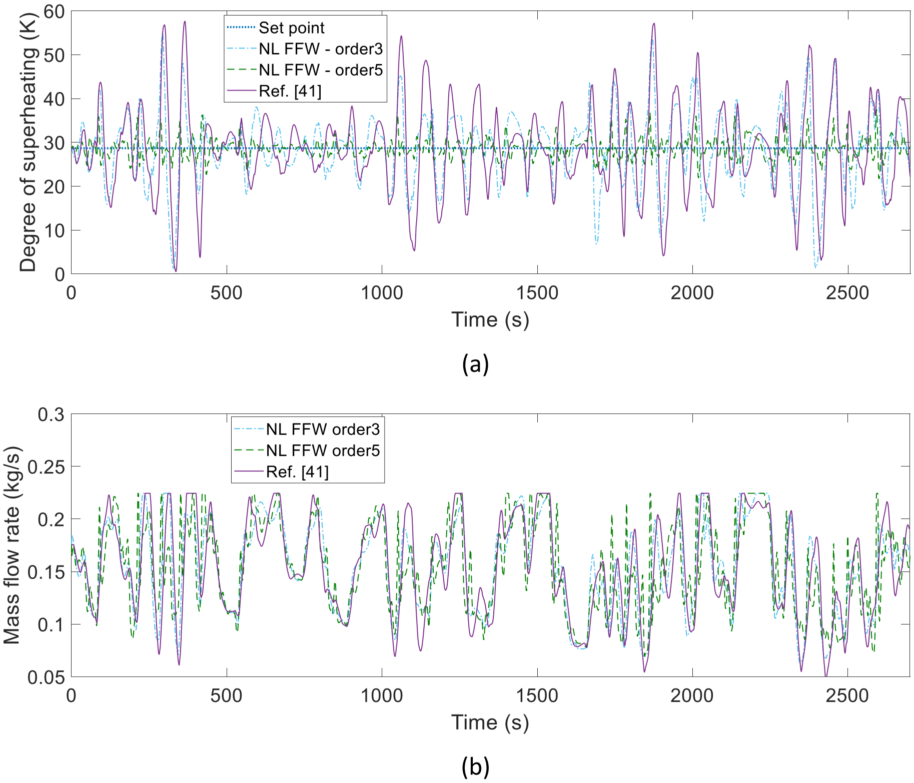

(a)

(b)

Fig. 16. Performance of nonlinear inversed-model dynamic feedforward: (a) degree of superheating and (b) mass flow rate of the pump of third-order and fifth-order models compared to the model presented in Ref. (Peralez et al., 2017).

to the third-order NL FFW case (1.2%/s vs 1.1%/s), but lower than the fifth-order case at 1.9%/s. On the other hand, the ARMSTE was 1.6 K higher than the third-order NL FFW and 7.8 K higher than the fifth-order NL FFW case. The main reasons for the poorer disturbance rejection performance of the model in Ref (Peralez et al., 2017). could lie in the assumption of the crossflow arrangement between the heat source and the ORC working fluid and the assumption of constant degree of superheating (equal to the set point) for the state observer and evaporation pressure control. The significant improvements of the NL FFW solutions compared to Ref (Peralez et al., 2017). highlight the benefits of the NL FFW solutions introduced in this work, thanks to the higher accuracy of the dynamic models on which they are based.

As is illustrated in Fig. 15, an outstanding disturbance rejection performance can be achieved by only employing PI feedback control with the tuning rule of Ref. (Skogestad, 2004), at the expense of a high cumulative controller effort. On the other hand, the ‘pidtune’ PI controller indicates a very high ARMSTE, but a low cumulative controller effort. Since the two PI solutions are at the opposite extremes of Fig. 15, it is possible that, by employing a different tuning, a better trade-off between the ARMSTE and the cumulative controller effort can be attained also for the PI feedback controllers. However, this would require a comprehensive analysis of the effects of tuning parameters on the performance PI feedback controllers. Dropping standard tuning rules and performing such a comprehensive analysis for each ORC design would result in a very computationally-intensive task. As shown in the present paper, the integration of feedforward control can support a PI feedback controller and lead to a better trade-off between the ARMSTE and the cumulative controller effort than achieved with the two PI feedback controllers. Lastly, it is important to highlight that the feedforward can integrate a PI controller independently from the tuning rule.

6. Conclusions

This work presented nonlinear dynamic inversed-model feedforward concepts to control the degree of superheating at the inlet of the organic Rankine cycle turbine by using high-order moving boundary models of the organic Rankine evaporator. High-order models include dynamic effects that are neglected by low-order models and have, therefore, the potential to improve significantly the controller performance. The main challenge was caused by the fact that moving boundary models of order higher than three are non-minimum phase and therefore do not satisfy the mathematical conditions required by the inversed-model feedforward. For this reason, novel approximations were introduced by modifying the mass accumulation term in the energy balance of the two-phase and vapor regions, thus avoiding the non-minimum phase behavior. The state estimation required by the nonlinear dynamic feedforward was carried out by using an Extended Kalman Filter with sample time of 0.5 s. The nonlinear feedforward solution was compared to classical proportional-integral feedback, static feedforward and linear dynamic inversed-model feedforward with gain-scheduling, using the evaporation pressure and the available waste heat rate as scheduling parameters. The controllers were tested on a waste heat profile available from the exhaust gas of a truck over a real driving cycle of 45 min.

The results of the numerical simulations show that a trade-off has to be found between the disturbance rejection performance of the controller, i.e. capability of keeping the degree of superheating close to the desired set point despite the rapid variations of waste heat, and the cumulative controller effort, i.e. how aggressive the controller acts on the pump to level off the variations of the available waste heat. While poor disturbance rejection performance can lead to inefficiencies and dangerous operation (i.e. liquid droplets at the turbine inlet), an excessively aggressive controller increases the risk of failure and reduces the lifetime of the pump. The results indicate that in general, the better the disturbance rejection performance of the controller, the higher the cumulative controller effort. Considering the feedback proportional-integral controllers, the ‘pidtune’ command from MATLAB® results in a gentler controller with relatively high absolute mean square tracking error in terms of the degree of superheating. The deviations from the set point largely decrease by using the proportional-integral tuning method described in Ref. (Skogestad, 2004); however, the cumulative controller effort also increases by 3.5 times. The results suggest that the static feedforward concept does not offer any advantages compared with the feedback ‘pidtune’ controller, because it results in higher absolute mean square tracking errors and a higher cumulative controller effort. This is also true for the linear feedforward with the evaporation pressure and available waste heat rate as scheduling parameters. These options could only achieve an absolute mean square tracking error 2.5 K higher than the ‘pidtune’ case with higher cumulative controller effort (from 0.8%/s to 1.9%/s and 2.1%/s).

On the other hand, the results for the nonlinear dynamic inversed-model feedforward controller highlight the capability of this solution to improve the disturbance rejection performance of the ‘pidtune’ feedback proportional-integral controller by reducing the absolute mean square tracking error from 10.8 K to only 2.2 K with the fifth-order model. The cumulative controller effort increases more moderately than the tuning rules used in Ref. (Skogestad, 2004), from 0.8%/s to 1.9%/s. The minimum degree of superheating increases from 0.7 K to 21.7 K. The nonlinear feedforward reduced-order models lie approximately (excluding the sixth-order model) on a straight line of negative slope, −772 K s, which highlights the counter-effect between the absolute mean square tracking error and the cumulative controller effort.

As demonstrated, the novel nonlinear feedforward models investigated in this work can lead to a significantly better trade-off between the disturbance rejection performance and the cumulative controller effort than that of the simple proportional-integral feedback control, allowing for continuous safe operation of the ORC unit, keeping it far from potentially dangerous operating regions, ensuring a more gentle operation and extending the component lifetime. Thereby, the nonlinear feedforward models constitute an effective, easy alternative to more complex, computationally intensive advanced control concepts, such as model predictive control. Nevertheless, it would be of interest to compare the performance of the novel nonlinear feedforward concepts proposed here with those of other control solutions, such as model predictive control, nonlinear model predictive control and simple proportional-integral controllers with optimized tuning parameters. Such analyses will be part of future work, including numerical as well as experimental investigations on a test rig that is currently under construction at the Department of Mechanical Engineering, Technical University of Denmark.

CRediT authorship contribution statement

Roberto Pili: Conceptualization, Data curation, Formal analysis, Funding acquisition, Investigation, Methodology, Project administration, Resources, Software, Supervision, Validation, Visualization, Roles/ . **Christoph Wieland:** Conceptualization, Methodology, Supervision, Funding acquisition, Visualization, Writing – review & editing. **Hartmut Spliethoff:** Conceptualization, Methodology, Funding acquisition, Supervision. **Fredrik Haglind:** Conceptualization, Methodology, Supervision, Project administration, Funding acquisition, Visualization, Writing – review & editing.

Declaration of competing interest

The authors declare that they have no known competing financial interests or personal relationships that could have appeared to influence the work reported in this paper.

Acknowledgments

This research was developed as part of the project “ACT-ORC: Advanced control of organic Rankine cycle for increased energy efficiency of heavy-duty trucks”, funded by the European Union’s Horizon 2020 research and innovation program under the Marie Sklodowska-Curie grant agreement no. 754462 (EuroTechPostdoc).

Appendix CSupplementary data

Supplementary data to this article can be found online at https://doi.org/10.1016/j.jclepro.2022.131470.

Nomenclature

Abbreviations

ARMSTE	Absolute Root Mean Square Tracking Error
CO	Condenser
EKF	Extended Kalman Filter
EVA	Evaporator
FFW	Feedforward (control)
FOPTD	First Order Plus Time Delay (model)
FV	Finite Volume (model)
GS	Gain Scheduling
LQR	Linear Quadratic Regulator
MB	Moving Boundary (model)
MPC	Model Predictive Control
NGC	Non-Gaussian Control
NL	Nonlinear (control)
ORC	Organic Rankine Cycle
P	Pump
PI	Proportional Integral (control)
PID	Proportional Integral Derivative (control)
T	Turbine
UKF	Unscented Kalman Filter

Symbols

$A(\mathrm{m}^2)$	Surface area

a(m)	Fin pitch
c_p(J/kgK)	Specific heat at constant pressure
c_W(J/kgK)	Specific heat of solid material (wall)
d(–)	Disturbance
d(m)	Tube diameter
f(–)	State function
G (s)(–)	Transfer function
g(–)	Output function
H(J)	Enthalpy
h(m)	Fin height
h(J/kg)	Specific enthalpy
k(1/Pa)	Controller proportional constant
k_T(kg/sK$^{0.5}$/Pa)	Turbine constant
l(m)	Tube length
M(kg)	Mass
$\dot{M}(s)$(kg/s)	Laplace transform of mass flow rate
$\dot{m}$(kg/s)	Mass flow rate
n_p(–)	Number of passes per row (tube side)
n_r(–)	Number of tube rows
n_{rp}(–)	Number of flow reversals per row
P(W)	Power
p(Pa)	Pressure
p_r(–)	Pressure ratio
$\dot{Q}$(W)	Heat transfer rate
Q_u(1/s)	Cumulative controller effort
R(K/W)	Thermal resistance
$SH(s)$(K)	Laplace transform of degree of superheating
s(m)	Fin thickness
s(–)	Laplace variable
T(K)	Temperature
$T(s)$(K)	Laplace transform of temperature
t(m)	Thickness
t(s))	Time
t_{np}(m)	Tube spacing between tubes in same row
t_{nr}(m)	Tube spacing between rows
u(J/kg)	Specific internal energy
V(m^3)	Volume
x(–)	State
$Y(s)$(–)	Laplace transform of output
y(–)	Output
y(–)	Volume fraction for each phase region
Z(–)	Compressibility factor

Greek symbols

α(W/m^{2}K)	Heat transfer coefficient
γ(–)	Volume fraction in two-phase region
η(–)	Efficiency
κ(–)	Ratio of specific heats
θ(–)	Scheduling parameter
ρ(kg/m^3)	Density
τ(–)	Power law exponent

Superscripts and subscripts

‘	filtered variable/saturated liquid
‘’	saturated vapor
A	Available
B	-boundary
D	Design
D1	disturbance 1
D2	disturbance 2
ExG	exhaust gas
F	working fluid
F	fins/finned
G	exhaust gas
I	Inner

In	inlet/input
Is	Isentropic
L	liquid phase
LV	two-phase
max	Maximum
min	Minimum
N	neighbor cell
O	outer bare (surface area)
out	outlet/output
SP	set point
sat	Saturation
tot	Total
U	Input
V	vapor phase
V	Volumetric
W	Wall
Wf	working fluid

Appendix A. Non-minimum phase systems

The explained feedforward concepts in section 4.2.3 cannot be used if the system is non-minimum phase. Examples of non-minimum phase systems are systems with time delay, which would require the controller to act in the past for the current desired set point, as for instance:

$$y(t) = u(t-L) \tag{A.1}$$

where L is the time delay. A similar case is the FOPTD model presented in section 4.2.2. Non-minimum phase systems can result from the opposite contribution of two responses having different time scales. For instance, the following system:

$$\begin{aligned} \dot{x}_1 &= -6.67\,x_1 - 2.08\,x_2 + 4\,u \\ \dot{x}_2 &= 2\,x_1 \qquad \leftrightarrow \; Y(s) = -5\frac{3s-5}{(s+5)(3s+5)}\,U(s) \\ y &= -2.5\,x_1 + 1.04\,x_2 \end{aligned} \tag{A.2}$$

is non-minimum phase. The positive zero at $5/3 = 1.67$ can be seen in the numerator of its transfer function in Eq. A.2. The system response to a unit step with initial state $(x_1,\ x_2) = (0{,}0)$ is the sum of the contributions of a steady-state term, a faster term causing a first positive peak, and a slower third term, which dominates after a few seconds and causes the decreasing part of the transient:

$$y(t) = 1 + 2\,e^{-5t} - 3\,e^{-1.67t} \tag{A.3}$$

The response is shown in Fig. A1a. An approximation can be carried out to avoid the inversed peak response, by the elimination of the positive zero in the transfer function. The inverse response can be avoided if the slower term becomes dominant also at the initial phase of the transient, e.g.:

$$Y'(s) = 25\frac{1}{(s+5)(3s+5)}\,U(s) \leftrightarrow Y'(s) = 25\frac{1}{(s+5)(3s+5)}\,U(s) \tag{A.4}$$

Fig. A.1b shows the response by using Eq. A.4. It can be seen that the inversed peak in the output y has now disappeared. The inverse of this system is now causal and stable. In order to make the inversion physically realizable, two filters are included in the numerator, without altering significantly the response, as shown in Fig. A1b. In this way, the inverse is minimum phase, and the feedforward can be realized.

$$Y'(s) = \frac{25}{1600}\,\frac{(s+40)^2}{(s+5)(3s+5)}\,U(s) \rightarrow U^{ff}(s) = \frac{1600}{25}\,\frac{(s+5)(3s+5)}{(s+40)^2}\,Y^{SP}(s) \tag{A.5}$$

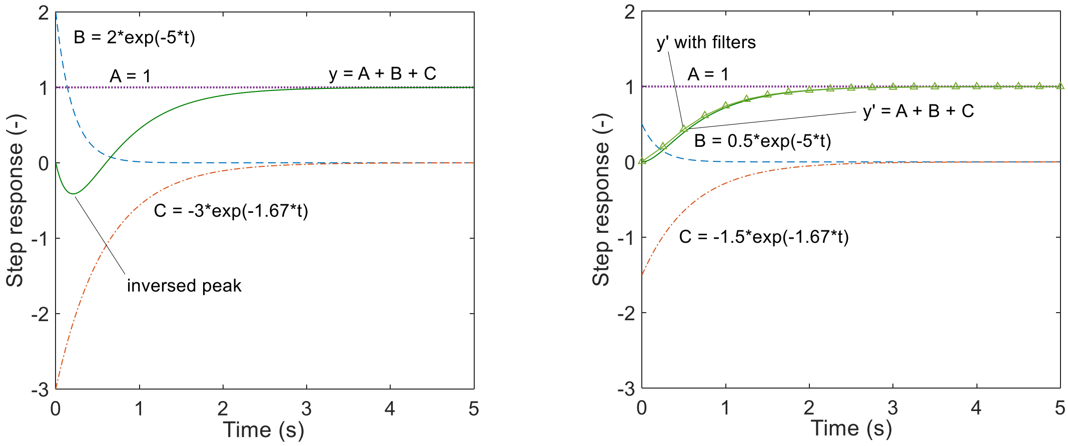

(a) (b)

Fig. A.1. Example of an approximation for a non-minimum phase system: (a) original step response and (b) approximation.

Appendix B. Supplementary data

The waste heat profile illustrated in Fig. 2 can be found as supplementary material to this document.

References

Amicabile, S., Lee, J.I., Kum, D., 2015. A comprehensive design methodology of organic Rankine cycles for the waste heat recovery of automotive heavy-duty diesel engines. Appl. Therm. Eng. 87, 574–585. https://doi.org/10.1016/j.applthermaleng.2015.04.034.

Andreasen, J.G., Meroni, A., Haglind, F., 2017. A comparison of organic and steam Rankine cycle power systems for waste heat recovery on large ships. Energies 10, 1–23. https://doi.org/10.3390/en10040547.

Aspen Technology, I., 2017. Aspen Exchanger Design and Rating.

Astrom, K.J., Hagglund, T., 2009. Pid Controllers 3–24. https://doi.org/10.1201/9781420019612.pt1.

Carraro, G., Pili, R., Lazzaretto, A., Haglind, F., 2021. Effect of the evaporator design parameters on the dynamic response of organic Rankine cycle units for waste heat recovery on heavy-duty vehicles. Appl. Therm. Eng. 198, 117496. https://doi.org/10.1016/j.applthermaleng.2021.117496.

Carstensen, A., Horn, A., Klammer, J., Gockel, J., 2019. Waste heat recovery in passenger cars and trucks. MTZ Worldw 80, 50–57. https://doi.org/10.1007/s38313-019-0014-3.

Corriou, J.-P., 2004. Process Control. Springer London, London. https://doi.org/10.1007/978-1-4471-3848-8.

de la Fuente, S.S., Greig, A.R., 2015. Making shipping greener: comparative study between organic fluids and water for rankine cycle waste heat recovery. J. Mar. Eng. Technol. 14, 70–84. https://doi.org/10.1080/20464177.2015.1077601.

Delgado, O., Lutsey, N., 2014. The U.S. SuperTruck Program: expediting the development of advanced heavy-duty vehicle efficiency technologies. Int. Counc. Clean Transp.

Desideri, A., Dechesne, B., Wronski, J., Van Den Broek, M., Gusev, S., Lemort, V., et al., 2016. Comparison of moving boundary and finite-volume heat exchanger models in the Modelica language. Energies 9. https://doi.org/10.3390/en9050339.

Dolz, V., Novella, R., García, A., Sánchez, J., 2012. HD Diesel engine equipped with a bottoming Rankine cycle as a waste heat recovery system. Part 1: study and analysis of the waste heat energy. Appl. Therm. Eng. 36, 269–278. https://doi.org/10.1016/j.applthermaleng.2011.10.025.

European Environmental Agency, 2018. Carbon Dioxide Emissions from Europe's Heavy-Duty Vehicles.

Feru, E., Willems, F., de Jager, B., Steinbuch, M., 2014. Modeling and control of a parallel waste heat recovery system for Euro-VI heavy-duty diesel engines. Energies 7, 6571–6592. https://doi.org/10.3390/en7106571.

Gaddis, E.S., Gnielinski, V., 2010. G8 Shell-Side Heat Transfer in Baffled Shell-And-Tube Heat Exchangers. VDI Heat Atlas. Springer Berlin Heidelberg, Berlin, Heidelberg, pp. 731–742. https://doi.org/10.1007/978-3-540-77877-6_41.

Grelet, V., Dufour, P., Nadri, M., Lemort, V., Reiche, T., 2015a. Explicit multi-model predictive control of a waste heat Rankine based system for heavy duty trucks. Proc IEEE Conf Decis Control. https://doi.org/10.1109/CDC.2015.7402105, 54rd IEEE: 179–84.

Grelet, V., Dufour, P., Nadri, M., Reiche, T., Lemort, V., 2015b. Modeling and control of Rankine based waste heat recovery systems for heavy duty trucks. IFAC-PapersOnLine 28, 568–573. https://doi.org/10.1016/j.ifacol.2015.09.028.

TLK Thermo GmbH. TILMedia Suite 2016.

TLK Thermo GmbH. TIL Suite 2016.

Hernandez, A., Desideri, A., Ionescu, C., Quoilin, S., Lemort, V., De Keyser, R., 2014. Increasing the efficiency of organic rankine cycle technology by means of multivariable predictive control. IFAC 19. https://doi.org/10.3182/20140824-6-za-1003.01796.

Hernandez, A., Desideri, A., Ionescu, C., Quoilin, S., Lemort, V., De Keyser, R., 2015. Experimental study of predictive control strategies for optimal operation of organic rankine cycle systems. In: 2015 Eur Control Conf ECC, pp. 2254–2259. https://doi.org/10.1109/ECC.2015.7330874, 2015.

Hernandez, A., Desideri, A., Ionescu, C., De Keyser, R., Lemort, V., Quoilin, S., 2016. Real-time optimization of organic Rankine cycle systems by extremum-seeking control. Energies 9. https://doi.org/10.3390/en9050334.

Imran, M., Haglind, F., 2019. Dynamic modelling and development of a reliable control strategy of organic Rankine cycle power systems for waste heat recovery on heavy-duty vehicles. In: ECOS 2019 - Proc 32nd Int Conf Effic Cost, Optim Simul Environ Impact Energy Syst, pp. 2409–2422.

Imran, M., Pili, R., Usman, M., Haglind, F., 2020. Dynamic modeling and control strategies of organic Rankine cycle systems: methods and challenges. Appl. Energy 276. https://doi.org/10.1016/j.apenergy.2020.115537.

Kandepu, R., Foss, B., Imsland, L., 2008. Applying the unscented Kalman filter for nonlinear state estimation. J. Process Control 18, 753–768. https://doi.org/10.1016/j.jprocont.2007.11.004.

Keller, M., Neumann, M., Eichler, K., Pischinger, S., Abel, D., Albin, T., 2020. Model predictive control for an organic rankine cycle system applied to a heavy-duty diesel engine. In: CCTA 2020 - 4th IEEE Conf Control Technol Appl, pp. 442–449. https://doi.org/10.1109/CCTA41146.2020.9206319.

Kind, M., Steiner, D., Chawla, J.M., Schröder, J.-J., Saito, Y., Auracher, H., et al., 2010. H3 Flow Boiling. VDI Heat Atlas. Springer Berlin Heidelberg, Berlin, Heidelberg, pp. 793–902. https://doi.org/10.1007/978-3-540-77877-6_124.

Koppauer, H., Kemmetmüller, W., Kugi, A., 2018. Model predictive control of an automotive waste heat recovery system. Control Eng. Pract. 81, 28–42. https://doi.org/10.1016/j.conengprac.2018.09.005.

Lemmon, E.W., Bell, I.H., Huber, M.L., McLinden, M.O., 2018. NIST Standard Reference Database 23: Reference Fluid Thermodynamic and Transport Properties-REFPROP, Version 10.0.

Lion, S., Michos, C.N., Vlaskos, I., Rouaud, C., Taccani, R., 2017. A review of waste heat recovery and Organic Rankine Cycles (ORC) in on-off highway vehicle Heavy Duty Diesel Engine applications. Renew. Sustain. Energy Rev. 79, 691–708. https://doi.org/10.1016/j.rser.2017.05.082.

Liu, X., Yebi, A., Anschel, P., Shutty, J., Xu, B., Hoffman, M., et al., 2017. Model predictive control of an organic rankine cycle system. Energy Proc. 129, 184–191. https://doi.org/10.1016/j.egypro.2017.09.109.

Luong, D., Tsao, T.C., 2014a. Linear Quadratic Integral control of an Organic Rankine Cycle for waste heat recovery in heavy-duty diesel powertrain. Proc. Am. Control Conf. 3147–52 https://doi.org/10.1109/ACC.2014.6858907.

Luong, D., Tsao, T., 2014b. Model predictive control of organic rankine cycle for waste heat recovery in heavy-duty diesel powertrain. In: Proc ASME 2014 Dyn Syst Control Conf DSCC2014, pp. 1–7.

Macchi, E., Astolfi, M., 2017. Organic Rankine Cycle (ORC) Power Systems. Elsevier. https://doi.org/10.1016/C2014-0-04239-6.

Marchionni, M., Bianchi, G., Karvountzis-Kontakiotis, A., Pesyridis, A., Tassou, S.A., 2018. An appraisal of proportional integral control strategies for small scale waste heat to power conversion units based on Organic Rankine Cycles. Energy 163, 1062–1076. https://doi.org/10.1016/j.energy.2018.08.156.

Mathworks®., 2019. Control System ToolboxTM, MATLAB®.

MathWorks®, 2019. Control System Designer App, MATLAB®.

MathWorks®. Simulink® 2019.

Meesenburg, W., Markussen, W.B., Ommen, T., Elmegaard, B., 2020. Optimizing control of two-stage ammonia heat pump for fast regulation of power uptake. Appl. Energy 271, 115126. https://doi.org/10.1016/j.apenergy.2020.115126.

Padula, F., Sandrini, R., Cominardi, G., 2012. Adaptive PI control of an organic Rankine cycle power plant. IFAC 2. https://doi.org/10.3182/20120328-3-it-3014.00078.

Peralez, J., Tona, P., Sciarretta, A., Dufour, P., Nadri, M., 2012. Towards model-based control of a steam Rankine process for engine waste heat recovery. IEEE Veh. Power Propuls. Conf. VPPC 2012, 289–294. https://doi.org/10.1109/VPPC.2012.6422718, 2012.

Peralez, J., Tona, P., Lepreux, O., Sciarretta, A., Voise, L., Dufour, P., et al., 2013. Improving the control performance of an organic rankine cycle system for waste heat recovery from a heavy-duty diesel engine using a model-based approach. Proc IEEE Conf Decis Control 6830–6836. https://doi.org/10.1109/CDC.2013.6760971.

Peralez, J., Nadri, M., Dufour, P., Tona, P., Sciarretta, A., 2017. Organic rankine cycle for vehicles: control design and experimental results. IEEE Trans. Control Syst. Technol. 25, 952–965. https://doi.org/10.1109/TCST.2016.2574760.

Petr, P., Schröder, C., Köhler, J., Gräber, M., 2015. Optimal control OF waste heat recovery systems applying nonlinear model predictive control (NMPC), pp. 1–10.

Pili, R., Castro Pastrana, J.D., Romagnoli, A., Spliethoff, H., Wieland, C., 2017. Working fluid selection and optimal power-to-weight ratio for ORC in long-haul trucks. Energy Proc. 129 https://doi.org/10.1016/j.egypro.2017.09.116.

Pili, R., Romagnoli, A., Jiménez-Arreola, M., Spliethoff, H., Wieland, C., 2019a. Simulation of Organic Rankine Cycle – quasi-steady state vs dynamic approach for optimal economic performance. Energy. https://doi.org/10.1016/j.energy.2018.10.166.

Pili, R., Romagnoli, A., Jiménez-Arreola, M., Spliethoff, H., Wieland, C., 2019b. Simulation of Organic Rankine Cycle – quasi-steady state vs dynamic approach for optimal economic performance. Energy 167, 619–640. https://doi.org/10.1016/j.energy.2018.10.166.

Pili, R., Eyerer, S., Dawo, F., Wieland, C., Spliethoff, H., 2020a. Development of a non-linear state estimator for advanced control of an ORC test rig for geothermal application. Renew. Energy 161, 676–690. https://doi.org/10.1016/j.renene.2020.07.121.

Pili, R., Eyerer, S., Dawo, F., Wieland, C., Spliethoff, H., 2020b. Development of a non-linear state estimator for advanced control of an ORC test rig for geothermal application. Renew. Energy. https://doi.org/10.1016/j.renene.2020.07.121.

Pili, R., Wieland, C., Spliethoff, H., Haglind, F., 2021. Model Predictive Control for Organic Rankine Cycle Systems on Heavy-Duty Trucks: Controller Tuning and Optimization. 6th Int. Semin. ORC Power Syst., Munich, Germany.

Quoilin, S., Aumann, R., Grill, A., Schuster, A., Lemort, V., Spliethoff, H., 2011. Dynamic modeling and optimal control strategy of waste heat recovery Organic Rankine Cycles. Appl. Energy 88, 2183–2190. https://doi.org/10.1016/j.apenergy.2011.01.015.

Quoilin, S., Broek, M Van Den, Declaye, S., Dewallef, P., Lemort, V., 2013. Techno-economic survey of organic rankine cycle (ORC) systems. Renew. Sustain. Energy Rev. 22, 168–186. https://doi.org/10.1016/j.rser.2013.01.028.

Rathod, D., Xu, B., Filipi, Z., Hoffman, M., 2019. An experimentally validated, energy focused, optimal control strategy for an Organic Rankine Cycle waste heat recovery system. Appl. Energy 256, 113991. https://doi.org/10.1016/j.apenergy.2019.113991.

EU, 2019. Regulation (EU) 2019/1242 of the European Parliament and of the Council of 20 June 2019 Setting CO2 emission performance standards for new heavy-duty vehicles and amending Regulations (EC) No 595/2009 and (EU) 2018/956 of the European Parliament. Off. J. Eur. Union L 198, 202–240.

Schmidt, T.E., 1945. La Production Calorifique des Surfaces Munies D'ailettes. Annex Du Bull L'institut Int Du Froid. Annex G-5.

Seitz, D., Gehring, O., Bunz, C., Brunschier, M., Sawodny, O., 2016. Dynamic model of a multi-evaporator organic rankine cycle for exhaust heat recovery in automotive applications. IFAC-PapersOnLine 49, 39–46. https://doi.org/10.1016/j.ifacol.2016.10.508.

Seitz, D., Gehring, O., Bunz, C., Brunschier, M., Sawodny, O., 2018. Model-based control of exhaust heat recovery in a heavy-duty vehicle. Control Eng. Pract. 70, 15–28. https://doi.org/10.1016/j.conengprac.2017.08.010.

Skogestad, S., 2004. Simple analytic rules for model reduction and PID controller tuning. Model. Identif. Control 25, 85–120. https://doi.org/10.4173/mic.2004.2.2.

Sprouse, C., Depcik, C., 2013. Review of organic Rankine cycles for internal combustion engine exhaust waste heat recovery. Appl. Therm. Eng. 51, 711–722. https://doi.org/10.1016/j.applthermaleng.2012.10.017.

Dassault Systèmes. FMI Kit for Simulink 2.0 2018.

Systèmes, Dassault, 2020. Dymola.

Teng, H., Regner, G., Cowland, C., 2007. Waste heat recovery of heavy-duty diesel engines by organic rankine cycle part II: working fluids for WHR-ORC. SAE Tech Pap. https://doi.org/10.4271/2007-01-0543.

Tona, P., Peralez, J., 2015. Control of Organic Rankine Cycle systems on board heavy-duty vehicles: a survey. IFAC-PapersOnLine 28, 419–426. https://doi.org/10.1016/j.ifacol.2015.10.060.

Usman, M., Imran, M., Lee, D.H., Park, B.S., 2017. Experimental investigation of off-grid organic Rankine cycle control system adapting sliding pressure strategy under proportional integral with feed-forward and compensator. Appl. Therm. Eng. 110, 1153–1163. https://doi.org/10.1016/j.applthermaleng.2016.09.021.

Vaupel, Y., Schulze, J.C., Mhamdi, A., Mitsos, A., 2021. Nonlinear model predictive control of organic Rankine cycles for automotive waste heat recovery: is it worth the effort? J. Process Control 99, 19–27. https://doi.org/10.1016/j.jprocont.2021.01.003.

Vetter, C., 2014. Thermodynamische Auslegung und transiente Simulation eines überkritischen Organic Rankine Cycles für einen leistungsoptimierten Betrieb. KIT Karsluhe.

Wei, D., Lu, X., Lu, Z., Gu, J., 2008. Dynamic modeling and simulation of an Organic Rankine Cycle (ORC) system for waste heat recovery. Appl. Therm. Eng. 28, 1216–1224. https://doi.org/10.1016/j.applthermaleng.2007.07.019.

Wu, X., Chen, J., Xie, L., 2019. Fast economic nonlinear model predictive control strategy of Organic Rankine Cycle for waste heat recovery: simulation-based studies. Energy 180, 520–534. https://doi.org/10.1016/j.energy.2019.05.023.

Xu, B., Rathod, D., Yebi, A., Filipi, Z., 2020a. A comparative analysis of real-time power optimization for organic Rankine cycle waste heat recovery systems. Appl. Therm. Eng. 164, 114442. https://doi.org/10.1016/j.applthermaleng.2019.114442.

Xu, B., Rathod, D., Yebi, A., Filipi, Z., 2020b. Real-time realization of Dynamic Programming using machine learning methods for IC engine waste heat recovery system power optimization. Appl. Energy 262, 114514. https://doi.org/10.1016/j.apenergy.2020.114514.

Zhang, J., Zhang, W., Hou, G., Fang, F., 2012a. Dynamic modeling and multivariable control of organic Rankine cycles in waste heat utilizing processes. Comput. Math. Appl. 64, 908–921. https://doi.org/10.1016/j.camwa.2012.01.054.

Zhang, J., Ren, M., Wang, H., 2012b. Minimum entropy control for non-linear and non-Gaussian two-input and two-output dynamic stochastic systems. IET Control Theory & Appl. 6, 2434–2441. https://doi.org/10.1049/iet-cta.2011.0791.

Zhang, J., Ren, M., Yue, H., 2016a. Constrained entropy-based temperature control of waste heat systems. Proc. World Congr. Intell. Control Autom. https://doi.org/10.1109/WCICA.2016.7578809, 2016-Septe:1992–8.

Zhang, J., Zhang, T., Lin, M., Hou, G., Li, K., 2016b. Multiple model predictive control for organic rankine cycle (ORC) based waste heat energy conversion systems. In: 2016 UKACC Int Conf Control UKACC Control, pp. 1–7. https://doi.org/10.1109/CONTROL.2016.7737577, 2016.

Zhang, J., Tian, X., Zhu, Z., Ren, M., 2018. Data-driven superheating control of organic Rankine cycle processes. Complexity. https://doi.org/10.1155/2018/4154019, 2018.

Zivi, S.M., 1964. Estimation of steady-state steam void-fraction by means of the principle of minimum entropy production. J. Heat Tran. 86, 247–251. https://doi.org/10.1115/1.3687113.